

Chemical tagging of the Ursa Major moving group

A northern selection of FGK stars [★]

H.M. Tabernero¹, D. Montes¹, J. I. González Hernández^{1,2,3}, and M. Ammler-von Eiff^{4,5}

¹ Dpto. Astrofísica, Facultad de CC. Físicas, Universidad Complutense de Madrid, E-28040 Madrid, Spain.
e-mail: htabernero@ucm.es

² Instituto de Astrofísica de Canarias, E-38205 La Laguna, Tenerife, Spain.

³ Universidad de La Laguna, Dept. Astrofísica, E-38206 La Laguna, Tenerife, Spain.

⁴ Thüringer Landessternwarte Tautenburg, Sternwarte 5, 07778, Tautenburg, Germany.

⁵ Max-Planck-Institut für Sonnensystemforschung, Justus-von-Liebig-Weg 3, 37077 Göttingen, Germany

Received 22 August, 2013; accepted 04 September, 2014

ABSTRACT

Context. Stellar kinematic groups are kinematical coherent groups of stars which might share a common origin. These groups spread through the Galaxy over time due to tidal effects caused by Galactic rotation and disc heating. However, the chemical information survives these processes.

Aims. The information provided by the analysis of chemical elements can reveal the origin of these kinematic groups. Here we investigate the origin of the stars that belong to the Ursa Major (UMa) Moving Group (MG).

Methods. We present high-resolution spectroscopic observations obtained from three different spectrographs of kinematically selected FGK stars of the Ursa Major moving group. Stellar atmospheric parameters (T_{eff} , $\log g$, ξ , and [Fe/H]) were determined using our own automatic code (STEPAR) which makes use of the sensitivity of iron equivalent widths (EWs) measured in the spectra. We critically compare the STEPAR results with other methods (T_{eff} values derived using the infrared flux method (IRFM) and $\log g$ values based on HIPPARCOS parallaxes). We derived the chemical abundances of 20 elements, and their [X/Fe] ratios of all stars in the sample. We perform a differential abundance analysis with respect to a reference star of the UMa MG (HD 115043). We have also carried out a systematic comparison of the abundance pattern of the Ursa Major MG and the Hyades SC with the thin disc stellar abundances.

Results. Our chemical tagging analysis indicates that the Ursa Major MG is less affected by field star contamination than other moving groups (such as the Hyades SC). We find a roughly solar iron composition [Fe/H] = 0.03 ± 0.07 dex for the finally selected stars, whereas the [X/Fe] ratios are roughly sub-solar except for super-solar Barium abundance.

Conclusions. We conclude that 29 out of 44 (i.e. 66%) candidate stars share a similar chemical composition. In addition, we find that the abundance pattern of the Ursa Major MG might be marginally different from that of the Hyades SC.

Key words. Galaxy: open clusters and associations: individual (Ursa Major, Ursa Major Moving Group) - Stars: fundamental parameters - Stars: abundances - Stars: kinematics and dynamics - Stars: late-type

1. Introduction

Stellar kinematic groups (SKGs) –superclusters (SCs) and moving groups (MGs)– are kinematic coherent groups of stars (Eggen 1994) that might share a common origin. Among them, the youngest SKGs are (see Montes et al. 2001a): the Hyades SC (600 Myr), the Ursa Major MG (Sirius SC, 300 Myr), the Local Association or Pleiades MG (20 to 150 Myr), the IC 2391 SC (35-55 Myr), and the Castor MG (200 Myr).

Since Olin Eggen introduced the concept of MGs and the fact that stars can maintain a kinematic signature over long periods of time, their existence (mainly in the case of the old MGs) has been disputed. The disruption of MGs is caused by the Galactic differential rotation. Furthermore, disc heating causes the velocity dispersion of disc stars to increase gradually with age (Wielen 1971).

[★] Based on observations obtained with the HERMES spectrograph at the *Observatorio del Roque de los Muchachos* (La Palma), the FOCES spectrograph at Calar Alto, and with the Coudé-Échelle spectrograph of the Alfred-Jensch-Teleskop at the Thüringer Landessternwarte Tautenburg.

The over density of stars in some regions of the Galactic velocity UV-plane may be the result of global dynamical mechanisms linked with the non-axisymmetry of the Galaxy (Famaey et al. 2005), namely the presence of a rotating central bar (e.g. Dehnen 1998; Fux 2001; Minchev et al. 2010), and spiral arms (e.g. Quillen & Minchev 2005; Antoja et al. 2009, 2011), or both (see Quillen 2003; Minchev & Famaey 2010).

Previous works show that different age sub-groups are located in the same region of the velocity plane as the classical MGs (Asiain et al. 1999) suggesting that both field stars and young coeval sub-groups can coexist in MGs (Famaey et al. 2007, 2008; Antoja et al. 2008; Klement et al. 2008; De Silva et al. 2008; Francis & Anderson 2009a,b; Zhao et al. 2009).

Using different age indicators (e.g. the lithium line Li I at 6707.8 Å, chromospheric activity) it is possible to quantify the contamination by younger or older field stars among late-type candidate members of a SKG (e.g. Montes et al. 2001b; Martínez-Arnáiz et al. 2010; López-Santiago et al. 2006, 2009; López-Santiago et al. 2010; Maldonado et al. 2010).

However, the detailed analysis of the chemical content (*chemical tagging*) is another powerful and complementary approach that provides clear constraints on the membership (Freeman & Bland-Hawthorn 2002; Mitschang et al. 2013). Unfortunately, chemical composition alone cannot provide the answers to the common origin unless previous information is available beforehand (i.e. information on kinematics). Regarding this approach, studies usually start from already known information (see Mitschang et al. 2013, and references therein), in order to fully exploit the *chemical tagging* approach.

Studies of open clusters such as the Hyades and Collinder 261 (Paulson et al. 2003; De Silva et al. 2006, 2007a, 2009) found high levels of chemical homogeneity, showing that chemical information is preserved within the stars, and that the possible effects of any external sources of pollution are negligible. Since chemical homogeneity is found among open clusters, it is possible to trace back dispersed clusters based on their chemical composition. In this sense *chemical tagging* was applied to the HR 1614 (De Silva et al. 2007b), to the Hercules stream (Bensby et al. 2007), Wolf 360 MG (Bubar & King 2010), and the Hyades SC (Pompéia et al. 2011; De Silva et al. 2011; Tabernero et al. 2012). These studies proved or disproved the common origin of these structures by using chemical abundance information. In particular, the Hyades SC is an interesting case. This MG is supposed to originate from the Hyades cluster and was an excellent test since there is a whole cluster to choose a reference star for the differential analysis. Tabernero et al. (2012) found that 46 % percent of Hyades SC members sharing similar abundances to the original Hyades cluster. On the contrary Pompéia et al. (2011) and De Silva et al. (2011) found that 10-15 % of the stars seem to originate from the Hyades cluster. These differences arise from the different sizes of the samples employed, ≈ 60 stars where analysed in Tabernero et al. (2012), whereas in Pompéia et al. (2011) and De Silva et al. (2011) analyse ≈ 20 stars. The comparison of these three studies shows that it is not possible to constrain the contamination level in moving groups until more complete samples are analysed. However, it would be still possible to find stars that may originate from a single cluster using the *chemical tagging* approach. The Hyades SC is not a unique case, De Silva et al. (2013) linked the open cluster IC2391 and the Argus association using chemical analysis.

In this paper, we apply the *chemical tagging* technique to a homogeneous sample of kinematically selected northern FGK Ursa Major MG candidates. This group has been previously investigated by Soderblom & Mayor (1993), King et al. (2003), King & Schuler (2005), Monier (2005), Ammler-von Eiff & Guenther (2009), Biazzo et al. (2012), D’Orazi et al. (2012). These studies demonstrate that their candidate members are consistent with a true MG of marginally sub-solar composition. Soderblom & Mayor (1993) find $[\text{Fe}/\text{H}] = -0.08 \pm 0.09$ dex, whereas Ammler-von Eiff & Guenther (2009) get a slightly higher value $[\text{Fe}/\text{H}] = -0.03 \pm 0.05$ dex. Finally, Biazzo et al. (2012) obtain $[\text{Fe}/\text{H}] = 0.01 \pm 0.03$, higher but consistent with previous measurements within the uncertainties. The study of individual abundances in Ammler-von Eiff & Guenther (2009) covers Fe and Mg. Biazzo et al. (2012) analyse 11 different chemical elements, whereas D’Orazi et al. (2012) also treat some s-process elements.

More importantly, the age of the Ursa Major MG is close to the time scale of the dissolution of open clusters (Wielen 1971). Therefore, this is an important case to study some aspects of the open cluster evolution and to apply the *chemical tagging* ap-

proach. In Sect. 2, we give details on the sample selection. Observations and data reduction are described in Sect. 3. Descriptions for the derivation of the stellar parameters and chemical abundances are provided in Sect. 4. Chemical abundances are given in Sect. 5 together with the discussion of the results. Finally in Sect. 6, we summarize our conclusions about UMa MG membership extracted from the *chemical tagging* approach.

2. Sample Selection

The sample analyzed in this paper (see Table ??) was selected using kinematical criteria based on U , V , and W Galactic velocities of a given target being approximately within 10 km s^{-1} of the mean velocity of the Ursa Major nucleus (King et al. 2003). We selected our kinematic candidates from Ammler-von Eiff & Guenther (2009), Holmberg et al. (2009), López-Santiago et al. (2010), Martínez-Arnáiz et al. (2010), and Maldonado et al. (2010). This candidate selection was later verified once more with the radial velocities coming from the spectroscopic data presented here (see Section 3).

After the first stage of selection based on kinematical criteria, we then discarded those stars that were unsuitable for our standard abundance analysis, namely stars cooler than K4 and hotter than F6, because for these stars we would have been unable to measure the spectral lines required for our particular abundance analysis. Stars with high rotational velocities (namely those greater than 15 km s^{-1}) were also discarded. In addition, we also removed spectroscopic binaries (SB2) to avoid confusion between the spectral lines of the two components during the analysis. After these considerations, we were left with 45 stars suitable for the present analysis.

We recalculated the Galactic velocities of our selected targets by employing the radial velocities and uncertainties derived by the HERMES spectrograph automated pipeline (Raskin et al. 2011). However, for stars observed with the FOCES and TLS spectrographs, we applied the cross-correlation technique using the routine `FXCOR` in IRAF¹, by adopting a solar spectrum as radial velocity template (the Kurucz solar *ATLAS* Kurucz et al. 1984). Those radial velocities were derived after applying the heliocentric correction to the observed velocity. Uncertainties were computed by `FXCOR` based on the fitted peak height and the antisymmetric noise, as described in Tonry & Davis (1979). The obtained radial velocities and their associated errors are given in Table ?. Proper motions and parallaxes were taken from the HIPPARCOS and Tycho catalogues (ESA 1997), the Tycho-2 catalogue (Høg et al. 2000), and the new reduction of the HIPPARCOS catalogue (van Leeuwen 2007).

Following the method described in Montes et al. (2001a) we determine the U , V , and W velocities. The Galactic velocities are in a right-handed coordinate system (positive in the directions of the Galactic centre, Galactic rotation, and the North Galactic Pole, respectively). Montes et al. (2001a) modified the procedures in Johnson & Soderblom (1987) to perform the velocity calculation and associated errors.

¹ IRAF is distributed by the National Optical Observatory, which is operated by the Association of Universities for Research in Astronomy, Inc., under contract with the National Science Foundation.

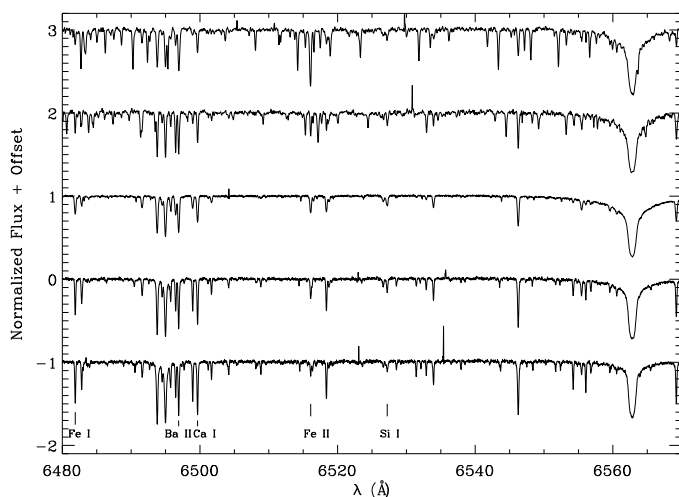


Fig. 1. High-resolution spectra for some representative stars from our sample (from top to bottom): HD 4048 (F8 V), HD 13829 (F8 V), HD 115043 (a G2 V reference star known to be a member of the Ursa Major nucleus), HD 76218 (G5 V), and HD 56168 (K0 V). Some lines used in the abundance analysis are highlighted in the bottom part of the diagram.

This modified program uses coordinates adapted to the epoch J2000 in the International Celestial Reference System (ICRS). The calculated velocities are given in Table ???. As some stars are observed with two or more spectrographs, we decided to run an internal consistency check to verify whether significant differences exist for different spectrographs. We find there is a small scatter of about 0.14 km s^{-1} . For these stars, final values of U , V , and W velocities were derived from the weighted average of their radial velocities, since the parallaxes and proper motion data are the same (see Table ??).

3. Observations

Spectroscopic observations (see Fig. 1) were obtained at the 1.2-m Mercator Telescope² at the *Observatorio del Roque de los Muchachos* (La Palma, Spain) in 2011–2012 with HERMES (High Efficiency and Resolution Mercator Echelle Spectrograph, Raskin et al. 2011) with the high-resolution mode. Additional spectra were taken in 2002–2004 with the 2.2-m telescope of the Centro Astronómico Hispano Alemán (CAHA) at Calar Alto with FOCES (operated by the Max-Planck-Institut für Astronomie Heidelberg and the Instituto de Astrofísica de Andalucía, CSIC), and the Coudé-Echelle spectrograph at 2-m *the Alfred-Jensch-Teleskop* at the Thüringer Landessternwarte in Tautenburg (TLS thereafter). Resolutions are 86,000 for HERMES, 40,000 for FOCES, and 67,000 for TLS. The wavelength range covered by the three spectrographs includes the range needed for our purposes: $\lambda 3600 \text{ \AA}$ to $\lambda 9000 \text{ \AA}$ approximately for HERMES and FOCES, $\lambda 4700 \text{ \AA}$ to $\lambda 7400 \text{ \AA}$ for TLS.

The typical signal-to-noise ratio (S/N) of the analyzed spectra is approximately 150 in the V band (at $\lambda 6070 \text{ \AA}$). We analysed single main-sequence stars (from F6 to K4), being 45 candi-

dates in total. Among them, there are 27 HERMES, 13 FOCES, and 17 TLS spectra (10 out of them are observed with more than one spectrograph). Our observations also include the reference star used in the differential abundance analysis (with respect to HD 115043). Additionally we took three solar spectra, one of the asteroid Vesta with HERMES, and two Moon spectra with FOCES and TLS.

The HERMES *echelle* spectra were reduced with the automatic pipeline (Raskin et al. 2011) at the Mercator Telescope. Additionally, the FOCES and TLS data comprise spectroscopic observations presented in Ammler-von Eiff & Guenther (2009). The IDL-based FOCES EDRS data reduction suite was adapted by Klaus Fuhrmann for use with the Tautenburg Coudé-Echelle spectrograph. The common steps of data reduction were followed (Horne 1986; McLean 1997) including bias subtraction, scattered light removal, order extraction, wavelength calibration using ThAr exposures, and division by flat-field exposures.

We later used several IRAF tasks to transform the observed spectra into a unique one-dimensional spectrum and applying the Doppler correction required to account for the radial velocity. In case several exposures were taken for the same star, we combined all of the individual spectra to obtain a unique spectrum at higher S/N .

4. Spectroscopic analysis

4.1. Stellar parameters

Stellar atmospheric parameters (T_{eff} , $\log g$, ξ , and $[\text{Fe}/\text{H}]$) were computed using the automatic code STEPAR (Tabernero et al. 2012). This automatic code employs a 2002 version of the MOOG code (Snedden 1973) and a grid of Kurucz ATLAS9 plane-parallel model atmospheres (Kurucz 1993). As damping prescription, we used the Unsöld approximation multiplied by a factor recommended by the Blackwell group (option 2 within MOOG). As line list we employed 300 Fe I–Fe II lines from Sousa et al. (2008). A typical star of our sample has 230–250 measurable Fe I and 20–25 Fe II lines. The STEPAR code iterates within the parameter space until the slopes of χ versus (*vs.*) $\log \epsilon(\text{Fe I})$ and $\log (EW/\lambda)$ vs. $\log \epsilon(\text{Fe I})$ are zero (excitation equilibrium). In addition, it imposes the ionization equilibrium, such that $\log \epsilon(\text{Fe I}) = \log \epsilon(\text{Fe II})$. We also imposed that the $[\text{Fe}/\text{H}]$ average of the MOOG output is equal to the metallicity of the atmospheric model. Tolerance values for these conditions are needed, thus reasonable limits must be defined. In STEPAR, we have chosen to iterate until the absolute value of the slope χ vs. $\log \epsilon(\text{Fe I})$ was $\leq 0.001 \text{ dex eV}^{-1}$, whereas the absolute value of the slope of $\log (EW/\lambda)$ vs. $\log \epsilon(\text{Fe I})$ was ≤ 0.002 . For the ionization balance we chose $|\log \epsilon(\text{Fe I}) - \log \epsilon(\text{Fe II})| \leq 0.005$.

STEPAR employs a Downhill Simplex Method (Press et al. 1992), and the problem function to minimize is a quadratic form composed of the excitation and ionization equilibrium conditions. Thus, STEPAR convergence towards the best solution in the stellar parameter space takes only a few minutes. We have tested that the obtained solution for a given star is independent of the initial set of parameters employed. Hence, we used the canonical solar values as initial input values ($T_{\text{eff}} = 5777 \text{ K}$, $\log g = 4.44 \text{ dex}$, $\xi = 1 \text{ km s}^{-1}$). In addition, we performed a $3\text{-}\sigma$ rejection of the deviant Fe I and Fe II lines after a first determination of the stellar parameters. Therefore, we re-run the STEPAR program again without the rejected lines.

The EW determination of Fe lines was carried out with the ARES³ code (Sousa et al. 2007). We followed the approach

³ The ARES code can be downloaded at <http://www.astro.up.pt/>

² Supported by the Fund for Scientific Research of Flanders (FWO), Belgium, the Research Council of K.U. Leuven, Belgium, the Fonds National Recherches Scientific (FNRS), Belgium, the Royal Observatory of Belgium, the Observatoire de Genève, Switzerland, and the Thüringer Landessternwarte Tautenburg, Germany.

of Sousa et al. (2008) to adjust the *rejt* parameter of ARES according to the *S/N* of each spectrum – the *rejt* parameter allows ARES to determine the stellar pseudocontinuum to fit the aimed *EW*s. The other ARES parameters we employed are *smoother* = 4 – the recommended parameter for smoothing the derivatives used for line identification, *space* = 3 – the wavelength interval (in Å) from each side of the central line to perform the *EW* computation, *lineresol* = 0.07 – the minimum distance for ARES to resolve lines, and *miniline* = 2 – minimum *EW* that will be printed in the ARES output. Details regarding the ARES parameters can be found in Sousa et al. (2007). In addition, ARES is able to measure automatically weak gaussian lines giving negligible systematic differences about 1-2 mÅ when compared against “manual” *EW* measurements (i.e. estimated with the IRAF *SPLOT* task, see Sousa et al. 2007; Ghezzi et al. 2010).

The uncertainties on the stellar parameters were computed taking into account one or more error sources for uncertainty for each parameter that will be added quadratically. The uncertainty on ξ is obtained using the slope of $\log \epsilon(\text{Fe I})$ vs. $\log (EW/\lambda)$. The uncertainty on T_{eff} is inferred by propagating two error sources added in quadrature: the slope $\log \epsilon(\text{Fe I})$ vs. χ and the variation introduced by the uncertainty of ξ .

We considered three error sources for $\log g$: the standard deviation of Fe II and the previous uncertainty on ξ and T_{eff} .

Finally, to determine the error in the Fe I, II abundance, we propagate the previously derived uncertainty on each stellar parameter plus the standard deviation of the Fe I, II abundances.

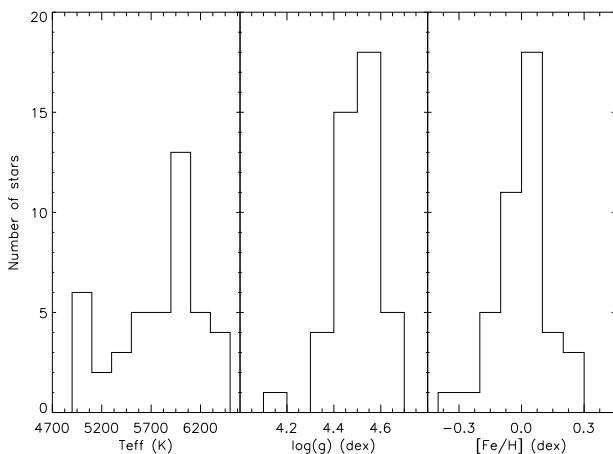


Fig. 2. Histograms for the determined values of T_{eff} , $\log g$, and $[\text{Fe}/\text{H}]$ of the candidate stars.

We have also performed the parameter determination of the solar spectra taken with the three different instruments. We are able to reproduce the solar parameters (see Table 1). Solar values for each chemical abundance, also given in Table 1, represent the zero-point for the solar abundance values. Ideally, abundance measurements in each solar reference spectrum should provide the same solar photospheric abundances for each spectrograph. However, small differences are noticed probably due to systematic effects, due to the different instrumental configurations, in the data taken with a specific instrument. These effects will likely apply to all candidate spectra of the UMa MG. Since our analysis is fully differential, the solar references are only used to convert the individual abundances (in a line-by-line basis) from $\log \epsilon(X)$ to $[X/\text{H}]$. Thus, the obtained chemical abundances will

Table 1. Stellar Parameters for our solar spectra (Moon and Vesta).

Spectrograph	HERMES	FOCES	TLS	average ^a	σ^b
T_{eff} (K)	5776	5778	5789	5781 ± 7	15
$\log g$	4.48	4.43	4.45	4.45 ± 0.03	0.05
ξ (km s ⁻¹)	0.97	1.08	1.05	1.03 ± 0.06	0.03
Element	$\log \epsilon(X)$				
Fe	7.46	7.47	7.48	7.47 ± 0.01	0.01
Na	6.37	6.36	6.34	6.36 ± 0.02	0.02
Mg	7.64	7.61	7.62	7.62 ± 0.02	0.06
Al	6.44	6.47	6.48	6.47 ± 0.02	0.02
Si	7.55	7.58	7.59	7.57 ± 0.02	0.06
Ca	6.34	6.35	6.33	6.34 ± 0.02	0.08
Sc	3.19	3.14	3.15	3.16 ± 0.03	0.06
Ti	4.99	5.01	5.02	5.01 ± 0.02	0.05
V	4.00	4.03	4.07	4.03 ± 0.04	0.07
Cr	5.66	5.66	5.68	5.67 ± 0.01	0.07
Mn	5.41	5.41	5.51	5.44 ± 0.06	0.05
Co	4.91	4.92	4.91	4.91 ± 0.01	0.03
Ni	6.26	6.26	6.26	6.26 ± 0.00	0.05
Cu	4.03	4.02	4.12	4.06 ± 0.06	0.08
Zn	4.54	4.57	4.57	4.56 ± 0.02	0.10
Y	2.17	2.15	2.16	2.15 ± 0.01	0.07
Zr	2.61	2.78	2.81	2.73 ± 0.10	0.14
Ba	2.35	2.44	2.47	2.42 ± 0.06	0.25
Ce	1.61	1.60	1.61	1.61 ± 0.01	0.08
Nd	1.47	1.53	1.51	1.50 ± 0.03	0.06

Notes. ^(a) Average value and standard deviation of the stellar parameters and $\log \epsilon(X)$.

^(b) Average internal uncertainties.

be referred to a solar spectrum corresponding to the instrument in which they were taken.

The obtained stellar parameters T_{eff} , $\log g$, ξ , $\log \epsilon(\text{Fe I})$, $\log \epsilon(\text{Fe II})$, and $[\text{Fe}/\text{H}]$ (using our solar references) are given in Table ?? (available online), together with the internal uncertainties in the stellar parameters. In Fig. 2, we show the histogram distributions of T_{eff} , $\log g$, and $[\text{Fe}/\text{H}]$ values. The effective temperature ranges approximately from 4800 K to 6500 K. The surface gravities of all stars in the sample are those typical of main sequence stars.

We also verify that systematic errors of the stellar parameters are small when we use different spectrographs for the same object. We find that differences between T_{eff} are less than 100 K, with a dispersion of 30 K. $\log g$ and $[\text{Fe}/\text{H}]$ show differences of less than 0.15 and 0.05 dex respectively. The dispersion is approximately 0.05 dex for surface gravity and 0.02 for $[\text{Fe}/\text{H}]$. These differences are quite small and they do not represent any significant difference when we derive stellar parameters from spectra taken with different *echelle* spectrographs. For these repeated spectra we employed an error-weighted average for their final stellar parameters. Then, the uncertainties are given as the mean value of the individual ones.

4.2. IRFM based effective temperatures

We have applied the infrared flux method (hereafter IRFM; Blackwell et al. 1990, and references therein) to the stellar sample presented in this work to also determine IRFM based effective temperatures, T_{IRFM} , as in González Hernández & Bonifacio (2009). We collected Johnson *V* photometric data from the General Catalogue of Photometric Data (GCPD Mermilliod et al. 1997). We also use

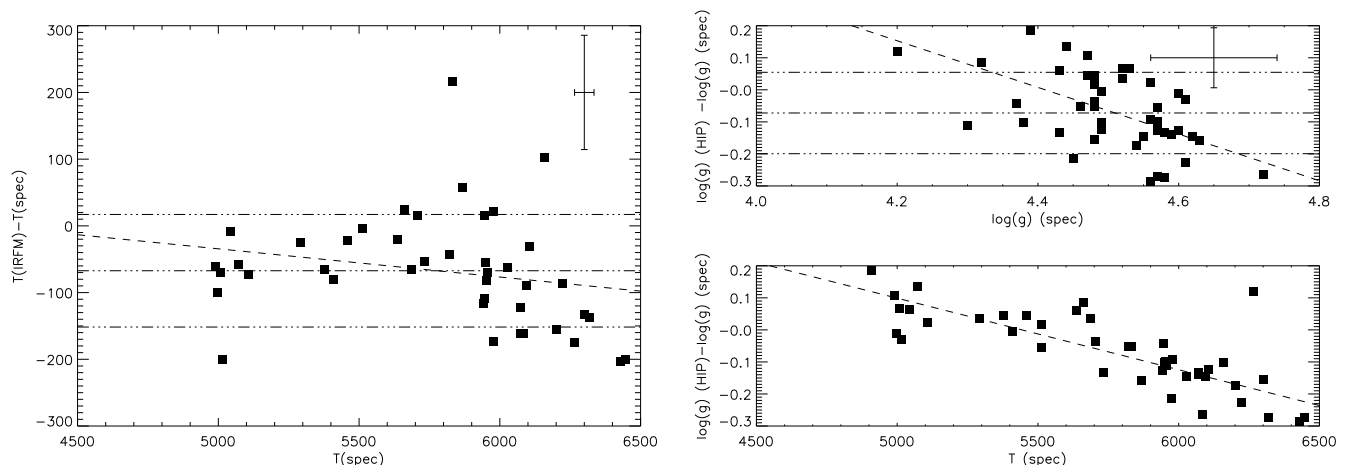


Fig. 3. Left panel: Comparison plot of $T_{\text{IRFM}} - T_{\text{eff}}$ vs T_{eff} . Right panel: Comparison plots of $\log g_{\text{Hip}} - \log g_{\text{spec}}$ vs $\log g_{\text{spec}}$ (top right), and $\log g_{\text{Hip}} - \log g_{\text{spec}}$ vs T_{eff} (bottom right). In all panels, dashed-dotted lines represent the mean difference value and the standard deviation. Dashed-lines represent the ordinary least squares fit through the points.

the Johnson V photometric data of HIPPARCOS-selected nearby stars from Koen et al. (2010). The T_{IRFM} and its uncertainty (ΔT_{IRFM}) were derived as the weighted average of the three individual temperatures and uncertainties derived from J, H, and K. For some stars of the sample we use the Tycho V magnitudes from the Tycho-2 catalogue (Høg et al. 2000), transformed into Johnson V using the expression given in Mamajek et al. (2002).

We also collected 2MASS infrared JHK_S photometry (Skrutskie et al. 2006) for the stars of the stellar sample. The extinction in each photometric band, A_i , is derived using the relation $A_i = R_i E(B - V)$, where R_i is given by the coefficients provided in McCall (2004). Reddening corrections, $E(B - V)$, were estimated from the dust maps of Schlegel et al. (1998), and corrected using the expressions given in Bonifacio et al. (2000a,b). Parallaxes are the same as those used in Section 2.

The photometric data and T_{IRFM} values are given in Table A.1. The stars γ Lep A/B and ξ Boo are perhaps too bright for 2MASS and thus the error on JHK_S magnitudes is too large to provide an accurate determination of T_{IRFM} . In addition, we estimated T_{IRFM} values assuming $E(B - V) = 0$ for comparison, $T_{\text{IRFM},0}$, although the effect is typically well within the uncertainties of T_{IRFM} . In Fig. 3 we compare the T_{IRFM} values with the spectroscopic T_{eff} values. We found a mean difference, alongside its standard deviation, of $T_{\text{IRFM}} - T_{\text{eff}} = -67 \pm 84$ K. The average error bar on T_{IRFM} is ~ 76 K. These differences may be slightly correlated with our T_{eff} , especially for the hottest stars of T_{eff} above 6000 K, this problem has been addressed in several studies (see Sousa et al. 2008; Ammler-von Eiff et al. 2009; Ammler-von Eiff & Guenther 2009; Mortier et al. 2013; Tsantaki et al. 2013), but it seems to be inherent to the differences between the IRFM method and the iron EW approach. We verify that the correlation between $T_{\text{IRFM}} - T_{\text{eff}}$ and T_{eff} is not significant. We find a correlation coefficient of $r = -0.21 \pm 0.15$ (illustrated by an ordinary least squares fit in Fig. 3). The goodness of fit is represented by the determination coefficient (given by $r^2 = 0.04 \pm 0.06$). We have also performed a t-test to assess the significance of the correlation coefficient (40 degrees of freedom). Thus, with a significance of 95% we find that the correlation is not significant for our spectroscopic T_{eff} . Also, the overall offset and scatter is small enough, possibly indicating that the T_{IRFM} is really similar to our spectroscopic T_{eff} . Thus,

we decided to adopt the spectroscopic T_{eff} for our abundance analysis.

4.3. HIPPARCOS based gravities

We derived HIPPARCOS gravities based on the obtained spectroscopic T_{eff} for the stellar sample in this study. This alternative gravity derivation requires the Johnson V photometric data discussed in Section 4.2, as well as the parallaxes discussed in Section 2. We use the web interface⁴ of the PARSEC5 isochrones (see Bressan et al. 2012) to derive the HIPPARCOS surface gravity (as in Sousa et al. 2008). The web interface only requires T_{eff} , V_{Johnson} , $[\text{Fe}/\text{H}]$, and the parallax, as well as their uncertainties to compute the desired HIPPARCOS surface gravities.

The photometric data and HIPPARCOS gravity values are given in Table A.1. In Fig. 3 we compare the $\log g_{\text{spec}}$ values with the spectroscopic $\log g_{\text{Hip}}$ values and we find a mean difference of $\log g_{\text{Hip}} - \log g_{\text{spec}} = -0.07 \pm 0.13$ dex. We find a correlation coefficient, for $\log g_{\text{Hip}}$ vs $\log g_{\text{spec}}$, $r = -0.49 \pm 0.15$ ($r^2 = 0.24 \pm 0.21$). In order to assess the significance of this correlation value we performed a t-test. As in Section 4.2 we used a confidence level of 95 % and 43 degrees of freedom. On the other hand for $\log g_{\text{Hip}}$ vs T_{spec} the correlation coefficient results in $r = -0.74 \pm 0.07$ ($r^2 = 0.55 \pm 0.10$). In both cases the correlation seems to be significant, with a 95 % confidence level, as it is shown in the right-hand panels of Fig. 3. Since the correlation is significant in the case of surface gravities, the effect on the chemical abundances must be considered (we refer the reader to the next section for further details).

On average, the stars tend to show lower $\log g_{\text{Hip}}$ than $\log g_{\text{spec}}$. The spectroscopic methodology we employ to derive surface gravities gives reliable T_{eff} estimates, but it is rather inefficient in estimating the surface gravity (see Sousa et al. 2008; Tsantaki et al. 2013; Mortier et al. 2013). For the cooler stars the EWs of the Fe II get weaker as T_{eff} drops. The hottest stars may also pose a problem in this sense, possibly due to arising difficulty in measuring the EW of the Fe II lines, thus losing sensitivity to surface gravity as these lines get weaker and less reliable with increasing temperatures (see bottom panel in Fig. 3).

⁴ <http://stev.oapd.inaf.it/cgi-bin/param>

As a complementary stellar parameter test, we create a $\log g_{\text{Hip}} - \log T_{\text{eff}}$ diagram show in Fig. 4. The selected stars fit within the depicted isochrones, being consistent with the isochrone for 0.3 Gyr (for a Ursa Major age reference, see King et al. 2003).

4.4. Chemical abundances

The selection of the chemical elements in this study is the same as in Tabernero et al. (2012) (see Table A.2) whose line list comes from a combination of atomic line data from González Hernández et al. (2010), Pompéia et al. (2011), and Sousa et al. (2008). A total of 20 elements were analyzed: Fe, the α -elements (Mg, Si, Ca, and Ti), the Fe-peak elements (Cr, Mn, Co, and Ni), the odd-Z elements (Na, Al, Sc, and V), Cu, Zn, and the s-process elements (Y, Zr, Ba, Ce, and Nd), see Tables A.3 and A.4. Chemical abundances were calculated using the *EW* method. The *EW*s were determined using the ARES code (Sousa et al. 2007), following the approach described in Sect. 4.1.

Once the *EW*s are measured, the analysis is carried out with the LTE MOOG code (2002 version, see Sneden 1973) using the ATLAS model corresponding to the derived atmospheric parameters. We determine chemical abundances (see Tables A.3 and A.4) relative to solar values using the spectrum of the asteroid Vesta, and two lunar spectra acting as solar reference for each instrument. We compute the mean of the line-by-line differences of each chemical element and candidate star with respect to our solar references (one for each spectrograph, see Table 1 for the solar reference elemental abundances). However, to avoid incorrect *EW* measurements (e.g. caused by a wrong continuum placement), we rejected those lines separated by more than a factor of two of the standard deviation (σ) from the median differential abundance derived for each line. Finally, in case of stars observed with two or three spectrographs, we simply take the average value of the available results. We have compared the solar abundances obtained with different instruments and the differences seem to be very small (0.10 dex or better) for the majority of the elements treated in this study (see Table 1).

The differential abundances were also determined to establish the membership of each stellar candidate using the star HD 115043 as reference (see Tables A.5 and A.6). The internal uncertainties of the derived stellar parameters (using STEPAR, see Sect. 4.1) are 28 K for T_{eff} , 0.07 dex for $\log g$, 0.05 km s^{-1} for ξ , and 0.03 dex for $[\text{Fe}/\text{H}]$. These average errors are in fact quite small, reflecting the relative internal precision of the obtained parameters. However, using these average values to assess the error bar on element abundance would be too optimistic. We found that systematic errors for T_{eff} and $\log g$ are 67 K and 0.07 dex respectively (see Sects. 4.2 and 4.3). Combining these systematic errors with our internal uncertainties, we obtained a total uncertainty of 72 K for T_{eff} and 0.10 dex for $\log g$.

However, for stars at $T_{\text{eff}} > 6000$ K, these combined uncertainties can raise up to 115 K and 0.27 dex. Therefore, in order to work with more conservative and reliable uncertainties, we used the values given by Neves et al. (2009), i.e.: $\Delta T_{\text{eff}} = \pm 100$ K, $\Delta \log g = \pm 0.30$ dex, $\Delta \xi = 0.50$ km s^{-1} , and $\Delta [\text{Fe}/\text{H}] = \pm 0.30$ dex. Using these uncertainties we derived the abundance sensitivities to changes in the stellar atmospheric parameters (see Table A.7 and A.9). Then, we combined the sensitivities to give an estimation of the error bar for $[\text{X}/\text{H}]$ and $[\text{X}/\text{Fe}]$. The final errors are usually driven by T_{eff} . However, some are dominated by ξ (e.g., for Ba) or by $\log g$ (e.g., for Ce and Nd).

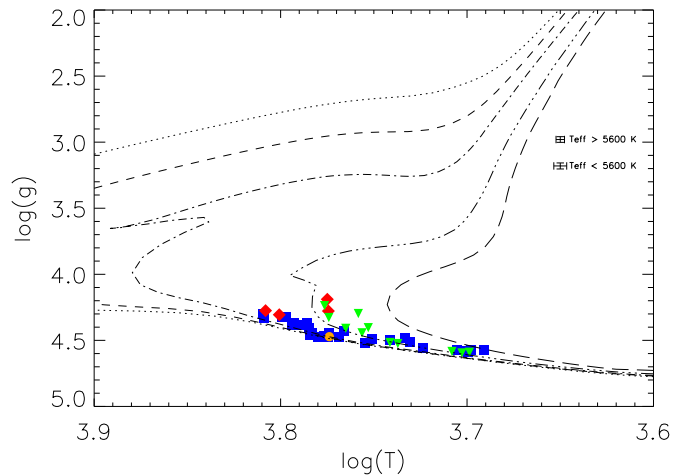


Fig. 4. Spectroscopic $\log T_{\text{eff}}$ vs. $\log g_{\text{Hip}}$ for the candidate stars. We have employed the Yonsei-Yale isochrones (Demarque et al. 2004) for $Z = 0.0$, and age = 0.1, 0.3, 0.5, 1, 4, and 13 Gyr (from left to right). Mean error bars are represented at the middle right. Blue squares represent stars selected as members by the *chemical tagging* approach, red diamonds represent those stars that have similar Fe abundances, but different values of other elements. The orange circle represents the reference star HD 115043. Inverted green triangles represent those stars that do not have similar Fe abundances (as well as dissimilar values of other elements). For the membership criterion we refer the reader to Section 5.

We performed a careful evaluation of the impact due to systematic errors on stellar atmospheric parameters derived with STEPAR. From subsections 4.2 and 4.3 the parameter most severely affected appears to be surface gravity. Thus, one might wonder whether its spectroscopic derivation may have an effect on the derived abundances. Therefore, we re-computed the differential abundances (with respect to HD 115043) with the HIPPARCOS surface gravities to verify possible differences. We find small differences at about hundredths of dex. For example, Ba and Ni remain nearly unaltered (with mean differences of 0.00 ± 0.02 and 0.01 ± 0.01 dex), whereas for Ca and Ce we find variations of -0.01 ± 0.03 dex, and 0.02 ± 0.05 dex respectively. As an additional check for systematic deviations, we compared two stars in common with Biazzo et al. (2012) and D’Orazi et al. (2012) (γ Lep A/B). Their abundances differ from ours by up to 0.11 dex in the worst case (i.e. for $[\text{Al}/\text{Fe}]$). In the best case, i.e. for $[\text{Ni}/\text{Fe}]$, they differ only by 0.01 dex. The above differences are similar to those due to the internal scatter (typically 0.01-0.10 dex). Finally, in order to be consistent with the previous study from Tabernero et al. (2012), we decided to use the stellar atmospheric parameters coming from STEPAR.

5. Discussion

We will compare our derived element abundances with those of thin disc stars (González Hernández et al. 2010, 2013) to determine whether our values follow Galactic trends. We will also verify the chemical homogeneity of the Ursa Major MG and whether some of the stars indeed have homogeneous abundances of all the considered elements.

5.1. Element abundances

The element abundances were determined in a fully differential way by comparing them with those derived for a solar spectrum (as stated in Section 4.1). The choice of elements is taken from Tabernero et al. (2012) (see also Table A.2) as explained in Section 4.4.

In the case of the α -elements (see Fig. 5) Si and Ca seem to follow the Galactic trends (see Bensby et al. 2005; Reddy et al. 2006; González Hernández et al. 2010, 2013). Mg is slightly sub-solar for stars around solar metallicity. Ti seems to follow the trends, but the scatter tends to increase as $[\text{Fe}/\text{H}]$ decreases for this narrow metallicity range. It has been suggested that Ti may suffer from NLTE effects, especially for cool stars. Therefore, to further check this issue, we have derived the difference $\log \text{Ti II} - \log \text{Ti I}$. For the coolest stars ($T_{\text{eff}} \leq 5500$ K), we obtain $\log \text{Ti II} - \log \text{Ti I} = 0.14 \pm 0.09$. For the hottest stars ($T_{\text{eff}} \geq 5500$ K), we obtain 0.06 ± 0.06 dex. At $1-\sigma$ level the difference is significant for the coolest stars ($T_{\text{eff}} \leq 5500$ K). Other studies have attributed that difference to Ti over-ionization (Lai et al. 2008; D’Orazi & Randich 2009; Biazzo et al. 2012; Adibekyan et al. 2012; De Silva et al. 2013). However, the total error bar for $\log \text{Ti I}$ is 0.21 dex (see Table A.7), maybe implying that the Ti abundance difference is not significant for the coolest stars, even if an observable offset is present. This difference may be connected to deviations either from excitation or ionization equilibrium (Adibekyan et al. 2012). Another possible explanation for the observed over-ionization could be an incorrect $T-\tau$ relationship in the adopted model atmospheres (Lai et al. 2008). Whereas this effect can be compensated for $[\text{Fe}/\text{H}]$ by changing ξ , it does not necessarily apply to other elements (Adibekyan et al. 2012).

For the iron peak elements (Cr, Mn, Co, and Ni, see Fig. 5), we find a small scatter in Ni and Cr. We note that most of the stars lie below the Galactic trend, and that Mn has a larger scatter. Ni, Mn, and Co show on average sub-solar values.

For the odd-Z elements (Na, Al, Sc, and V, see Fig. A.1), Na and Al seem to be sub-solar in composition as it happens for some Fe-peak elements. A high dispersion is observed for Sc, however it seems compatible with the Galactic trend. We confirm a large dispersion for V, which some authors interpret as a NLTE effect (e.g. Bodaghee et al. 2003; Gilli et al. 2006; Neves et al. 2009) affecting mostly the coolest stars. Vanadium lines are indeed difficult to measure and may require very high signal-to-noise data.

Cu, Zn, and the s-process elements (Y, Zr, Ba, Ce, and Nd, see Figs. A.1) follow similar trends to those seen in solar analogues (González Hernández et al. 2010). We find some enhancement for Ba above the solar level as observed in open clusters and moving groups with ages below 1 Gyr. D’Orazi et al. (2009) and D’Orazi et al. (2012) showed that for 0.3 Gyr (the Ursa Major attributed age, see King et al. 2003; Ammler-von Eiff & Guenther 2009) one might expect to find 0.2-0.3 dex for $[\text{Ba}/\text{Fe}]$. In our sample, we find similar values for a majority of Ursa Major MG stars (see Fig. A.1). The Ba over-abundance is not reflected for Y, Zr, and Ce. Although the scatter is relatively large the average abundance values are not enhanced. Cu and Zn seem to be solar in spite of the high scatter found for these elements. Nd seems to be really high compared to the Galactic abundance pattern, although there are some stars following the Galactic trend. At solar metallicities, however, it raises up to 0.2 dex. The higher than solar Nd abundance of many Ursa Major candidate stars does not endanger the subse-

quent differential analysis, since the reference star HD 115043 is also enhanced ($[\text{Nd}/\text{Fe}] = 0.15 \pm 0.03$, see Table A.4).

5.2. Differential abundances with respect to HD 115043

We determine differential abundances $\Delta[X/\text{H}]$ by comparing our measured abundances with those of a reference star known to be a member of the Ursa Major nucleus (HD 115043, see King et al. 2003) on a line-by-line basis. The candidate selection within the sample was determined by applying a one root-mean-squared (rms, thereafter) rejection over the median for almost every chemical element studied. The rejection process considers the rms in the abundances of the sample for each element. At first, we discarded every star that deviates by more than 1-rms from the median abundance denoted by the dashed-dotted lines in Figs. 6, and A.3. The initial rms values considered during the candidate selection are given in Table 2.

The initial 1-rms rejections lead to the identification of 15 candidate members. We subsequently apply a more flexible criterion allowing stars to become members when their abundances were within the 1-rms interval for 90 % of the elements considered and the remaining 10 % within the 1.5-rms interval (i.e. 18 elements and 2 elements respectively). The final rms is referred to the selected candidates of the Ursa Major moving group. The error analysis considers only the standard deviation in the line-by-line differences. Using this flexible approach allows us to find 29 members that may share similar abundances among the whole sample containing 44 stars (i.e., a 66%).

This more flexible rms-based analysis was made in order to identify the degree at which the sample is homogeneous, and to account for the likely contamination of the sample by field stars. Therefore, to assess this degree of homogeneity one must take into account the number of stars that lie within 1-rms, 1.5-rms, 2-rms, and 3-rms intervals (see Table 3). The last three columns of Table ?? give information about membership based on the differential abundances (with respect to HD 115043) of Fe and the other elements following these criteria. Combining the pure 1-rms rejection and the more flexible criteria we obtain that from 34% to 66% of the candidates are members of UMa, for a pure 1-rms rejection and the flexible criterion, respectively. The rms of the final selection for different elements ranges about 0.1 dex to 0.05 dex. We find that Si, Ca, Cr, Fe, and Ce exhibit an internal dispersion equal or better than 0.08 dex. On the other hand, Na, Mg, Ti, Ni, Zn, Zr, and Nd display a dispersion of less than 0.1 dex. The remaining elements have a rms scatter around 0.1 dex (see Table 2). Interestingly, the present chemical analysis can eliminate some outliers in the space velocity diagram (see Fig 7). In addition, our final set of selected candidates tends to concentrate nearby the mean velocity of the Ursa Major MG.

As a final test, we compared the Hyades SC abundances (Tabernero et al. 2012) and thin disc (González Hernández et al. 2010) with those of UMa (see Fig. 8). For the thin disc, each value is derived from the average of those stars within one σ around the $[\text{Fe}/\text{H}]$ of each MG. It is interesting to check whether the two moving groups have different abundance patterns. Some of the 20 individual abundances seem to be marginally distinguishable, with a few noticeable exceptions, namely Ca, V, Y, Ba, and Zr. The other elements might behave differently for the two groups, the Ursa Major MG being less metallic (nearly solar) than the Hyades SC (super-solar composition).

Different abundance patterns can indicate a different formation site (Freeman & Bland-Hawthorn 2002). Therefore, it would be possible to distinguish different stars from different moving groups when using the *chemical tagging* approach. In

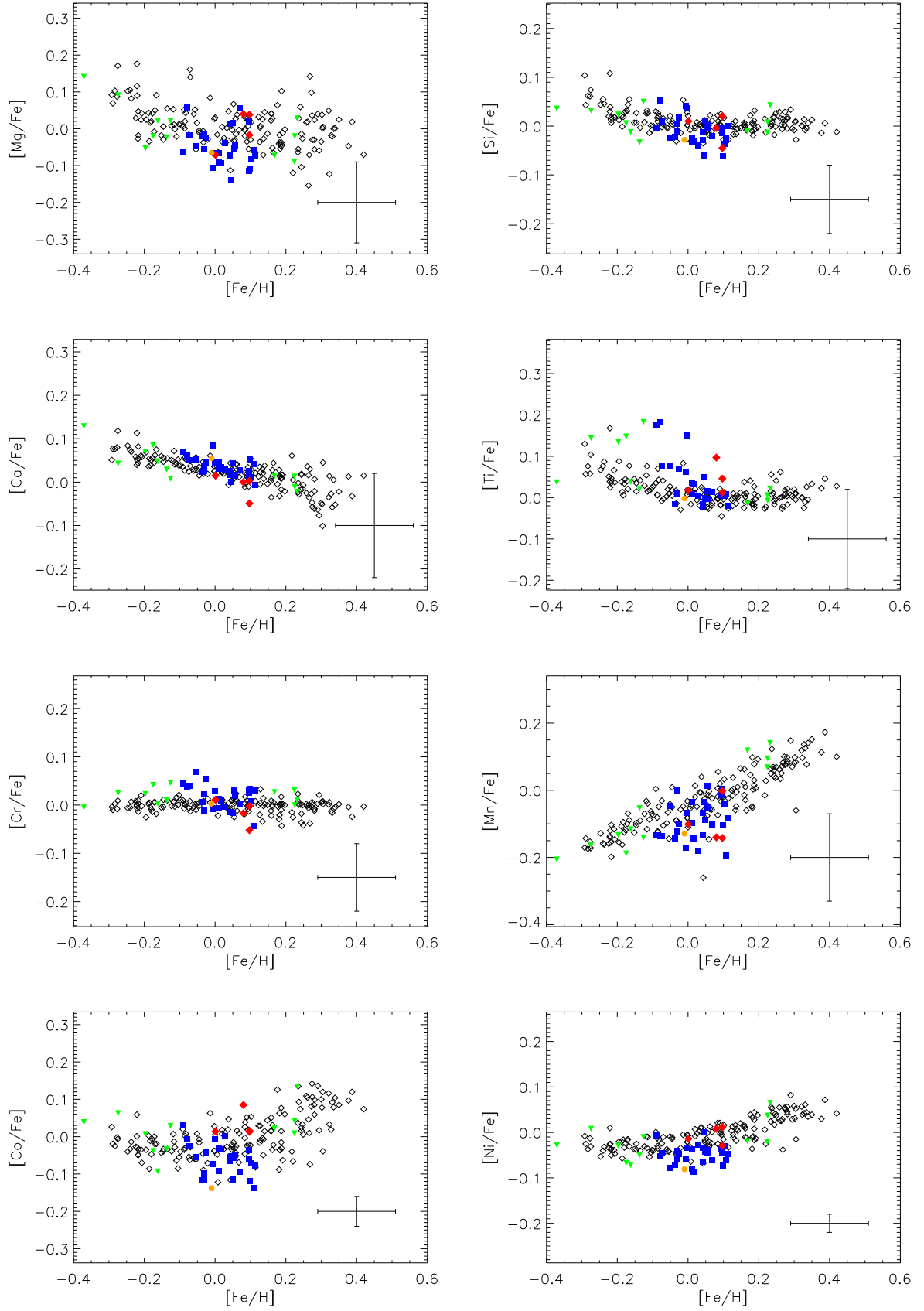


Fig. 5. $[X/Fe]$ vs. $[Fe/H]$ for the α -elements (Mg, Si, Ca, and Ti), and the Fe-peak elements (Cr, Mn, Co, and Ni): open diamonds represent the thin disc data (González Hernández et al. 2010, 2013), red diamonds are our stars compatible to within 1-rms with the Fe abundance but not for all elements, blue squares are the candidates selected to become members of the Ursa Major MG. Inverted green triangles show incompatible stars. The reference star, HD 115043, known to be a member of the Ursa Major nucleus is marked with an orange circle. Also, representative error bars are displayed in each graph.

Table 2. Median differential abundances (with respect to HD 115043), and both initial and final rms values for all considered elements.

Element	$\Delta [X/H]$	rms_o	rms_f
Na	0.03	0.15	0.09
Mg	0.02	0.13	0.08
Al	0.10	0.15	0.11
Si	0.06	0.12	0.08
Ca	0.00	0.11	0.05
Sc	0.05	0.17	0.12
Ti	0.07	0.12	0.08
V	0.10	0.18	0.14
Cr	0.04	0.11	0.06
Mn	0.05	0.20	0.11
Co	0.09	0.17	0.11
Ni	0.07	0.15	0.09
Fe	0.04	0.12	0.07
Cu	0.13	0.22	0.17
Zn	0.03	0.15	0.09
Y	0.09	0.15	0.10
Zr	0.01	0.16	0.09
Ba	-0.14	0.22	0.15
Ce	-0.01	0.10	0.06
Nd	-0.01	0.15	0.08

Table 3. Percentage analysis based on the rejection level of the differential abundances (with respect to HD 115043).

rms	#stars	%stars
1.0	15	34
1.5	31	71
2.0	36	82
2.5	38	86
3.0	41	93

spite of the fact that the abundances seem to be different from those of field stars, the internal dispersion does not give a clear hint on any palpable difference. We also note that a detailed treatment of several different elements is important to have a good picture of the composition of moving groups. In conclusion, the two MGs might behave differently in the abundance space.

6. Conclusions

We have computed the stellar parameters and their uncertainties for 45 Ursa Major MG candidate stars, and obtained their chemical abundances for 20 elements (Fe, Na, Mg, Al, Si, Ca, Ti, V, Cr, Mn, Co, Fe, Ni, Cu, Zn, Y, Zr, Ba, Ce, and Nd), using a fully differential abundance approach with solar spectra of Vesta and the Moon as solar references.

We derive the Galactic space velocity components for each star and use them to check the original selection based on Galactic velocities (Montes et al. 2001a; López-Santiago et al. 2010), which was then improved using the radial velocities derived from our data. We employ the new HIPPARCOS proper motions and parallaxes (Høg et al. 2000; van Leeuwen 2007) using the procedures described in Montes et al. (2001a). To perform a preliminary consistency check, we analysed the U , V , and W Galactic velocities (see Fig. 7) of the final selected stars to not include any outliers in V .

As a complementary test of the stellar parameters, we compile a $\log g$ vs. $\log T_{\text{eff}}$ diagram to verify the consistency of the method employed to determine the stellar parameters. This diagram shows that most of the stars fall on the isochrone for the Ursa Major attributed age (0.3 Gyr, see King et al. 2003;

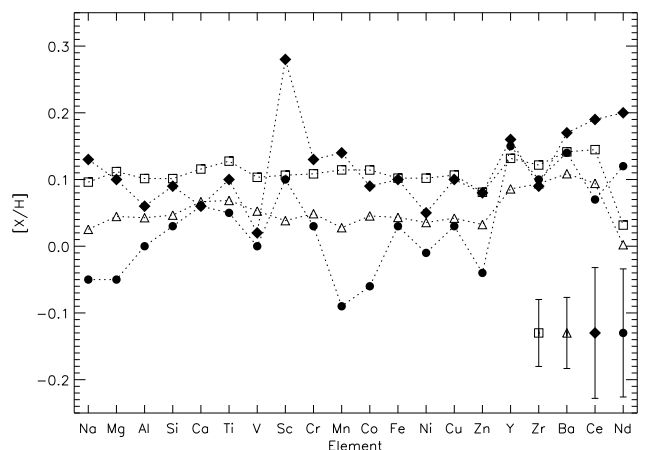


Fig. 8. Elemental abundances for the Hyades SC (filled diamonds, see Tabernero et al. 2012) and the Ursa Major MG (filled circles). Thin disc abundance values for field solar analogues (González Hernández et al. 2010) are represented by open triangles (at Ursa Major MG [Fe/H]) and open squares (at the Hyades SC [Fe/H]). Right bottom error bars represent the standard deviation. Dotted lines simply join the points for each moving group.

Ammler-von Eiff & Guenther 2009). This is an important but insufficient condition to ascertain that they have a common origin. The differential abundance analysis (*chemical tagging*) shows that the finally 29 selected stars are compatible with the accepted age isochrone, as expected if they have evaporated from a single star forming event. The membership percentage that we find in this work (66%) may indicate that the Ursa Major MG is likely to originate from a dispersing cluster. This result was also pointed out by other studies (such as King et al. 2003; King & Schuler 2005; Ammler-von Eiff & Guenther 2009, and references therein). Furthermore, we also verify that different moving groups (Hyades SC and Ursa Major) might be distinguished by the individual element abundances (see Fig. 8).

A yet more detailed analysis of different age indicators and chemical homogeneity is in progress and will be presented in future publications. This analysis will lead to a more consistent means of confirming a list of candidate members from the abundance analysis.

Acknowledgements. H.M.T and D.M acknowledge financial support from the Universidad Complutense de Madrid (UCM), the Spanish Ministry of Economy and Competitiveness (MINECO) from projects AYA2011-30147-C03-02, and The Comunidad de Madrid under PRICIT project S2009/ESP-1496 (Astro-Madrid). H.M.T also acknowledges the financial support of the Spanish Ministry of Economy and Competitiveness (MINECO) under grants BES-2009-012182 and EEBB-I-12-04038. J.I.G.H. acknowledges financial support from the Spanish Ministry project MINECO AYA2011-29060, and also from the Spanish Ministry of Economy and Competitiveness (MINECO) under the 2011 Severo Ochoa Program MINECO SEV-2011-0187. M.A. acknowledges help by Klaus Fuhrmann who adapted the FOCES reduction pipeline for use with the Tautenburg Coudé-Echelle spectrograph. In addition, M.A. thanks Eike W. Guenther for providing observing time with the 2m telescope in Tautenburg. Furthermore, M.A. would like to thank the staff at the Calar Alto and Tautenburg observatories. M.A. is supported by DLR (Deutsches Zentrum für Luft- und Raumfahrt) under the project 50 OW 0204. We would like to thank the anonymous referee for helpful comments and corrections. This publication makes use of data products from the Two Micron All Sky Survey, which is a joint project of the University of Massachusetts and the Infrared Processing and Analysis Center/California Institute of Technology, funded by the National Aeronautics and Space Administration and the National Science Foundation. This research has made use of the SIMBAD database, operated at the CDS, Strasbourg, France.

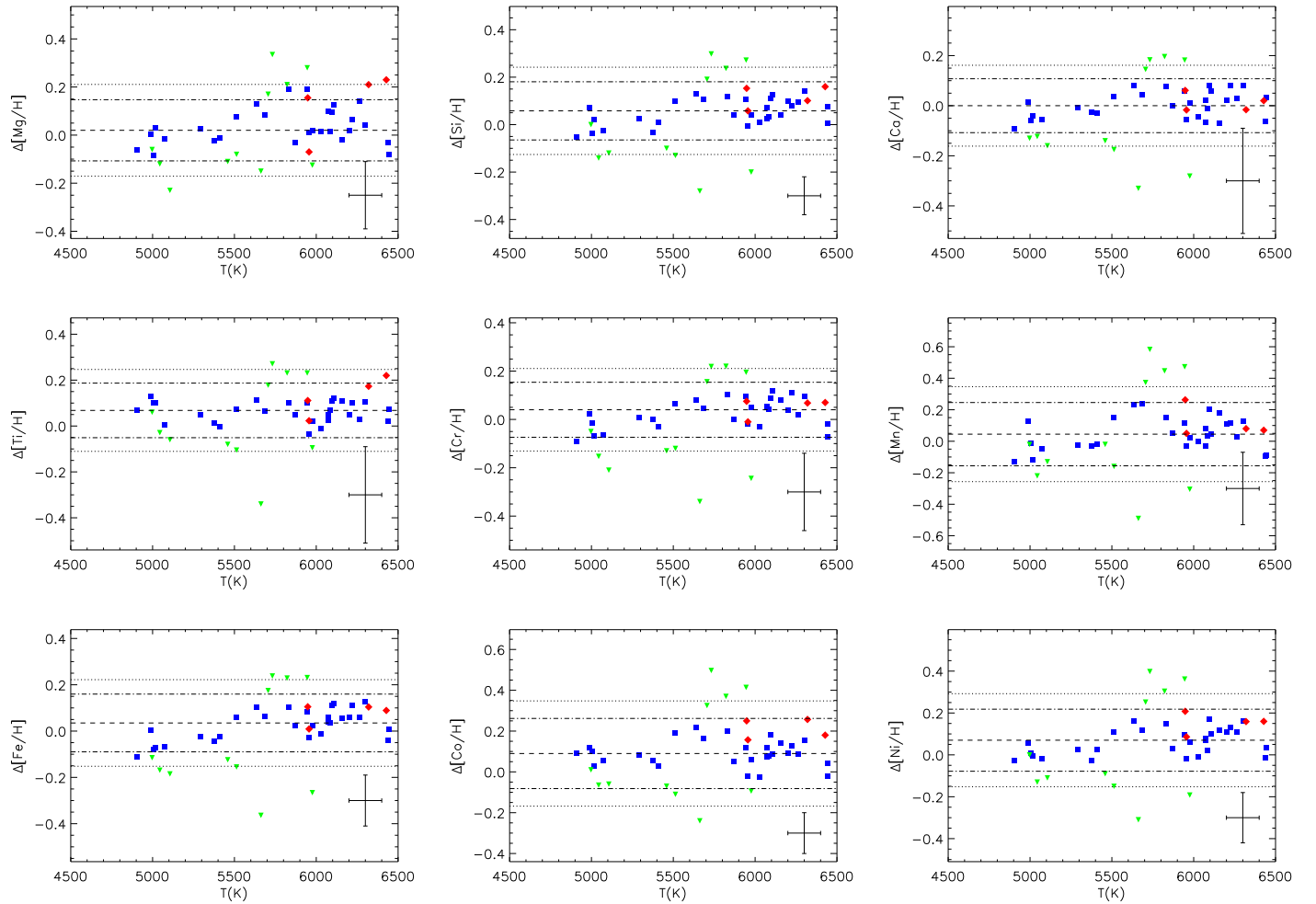


Fig. 6. $\Delta[X/H]$ differential abundances (with respect to HD 115043) for the α -elements (Mg, Si, Ca, and Ti), Fe, and the Fe-peak elements (Cr, Mn, Co, and Ni) vs. T_{eff} . Dashed-dotted lines represent 1-rms over and below the median for our sample, whereas dotted lines represent the 1.5-rms level. Dashed lines represent the mean differential abundance. The meaning of the symbols is the same as in Fig. 5

References

- Adibekyan, V. Z., Sousa, S. G., Santos, N. C., et al. 2012, *A&A*, 545, A32
 Ammler-von Eiff, M., Santos, N. C., Sousa, S. G., et al. 2009, *A&A*, 507, 523
 Ammler-von Eiff, M., & Guenther, E. W. 2009, *A&A*, 508, 677
 Antoja, T., Figueras, F., Fernández, D., & Torra, J. 2008, *A&A*, 490, 135
 Antoja, T., Valenzuela, O., Pichardo, B. et al. 2009, *ApJ*, 700, L78
 Antoja, T., Figueras, F., Romero-Gómez, M. et al. 2011, *MNRAS*, 418, 1423
 Asiain, R., Figueras, F., Torra, J., & Chen, B. 1999, *A&A*, 341, 427
 Bensby, T., Feltzing, S., & Lundström, I. 2003, *A&A*, 410, 527
 Bensby, T., Feltzing, S., Lundström, I., & Ilyin, I. 2005, *A&A*, 433, 185
 Bensby, T., Oey, M. S., Feltzing, S., & Gustafsson, B. 2007, *ApJ*, 655, L89
 Biazzo, K., D’Orazi, V., Desidera, S., et al. 2012, *MNRAS*, 427, 2905
 Blackwell, D. E., Petford, A. D., Arribas, S., Haddock, D. J., & Selby, M. J. 1990, *A&A*, 232, 396
 Bodaghee, A., Santos, N. C., Israelian, G., & Mayor, M. 2003, *A&A*, 404, 715
 Bonifacio, P., Caffau, E., & Molaro, P. 2000, *A&AS*, 145, 473
 Bonifacio, P., Monai, S., & Beers, T. C. 2000, *AJ*, 120, 2065
 Bressan, A., Marigo, P., Girardi, L., et al. 2012, *MNRAS*, 427, 127
 Bubar, E. J., & King, J. R. 2010, *AJ*, 140, 293
 Dehnen, W. 1998, *AJ*, 115, 2384
 Demarque, P., Woo, J.-H., Kim, Y.-C., & Yi, S. K. 2004, *ApJS*, 155, 667
 De Silva, G. M., Sneden, C., Paulson, D. B. et al. 2006, *AJ*, 131, 455
 De Silva, G. M., Freeman, K. C., Asplund, M. et al. 2007, *AJ*, 133, 1161
 De Silva, G. M., Freeman, K. C., Bland-Hawthorn, J., Asplund, M., & Bessell, M. S. 2007, *AJ*, 133, 694
 De Silva, G. M., Freeman, K. C., Bland-Hawthorn, J., & Asplund, M. 2008, *ASP Conference Series*, Vol. 396, 2008 J. G. Funes, S.J., and E. M. Corsini, eds., arXiv:0810.3346
 De Silva, G. M., Freeman, K. C., & Bland-Hawthorn, J. 2009, *PASA*, 26, 11
 De Silva, G. M., Freeman, K. C., Bland-Hawthorn, J. et al. 2011, *MNRAS*, 415, 563
 De Silva, G. M., D’Orazi, V., Melo, C., et al. 2013, *MNRAS*, 431, 1005
 D’Orazi, V., Magrini, L., Randich, S., et al. 2009, *ApJ*, 693, L31
 D’Orazi, V., & Randich, S. 2009, *A&A*, 501, 553
 D’Orazi, V., Biazzo, K., Desidera, S., et al. 2012, *MNRAS*, 423, 2789
 Eggen, O. J. 1984, *ApJS*, 55, 597
 Eggen, O. J. 1989, *PASP*, 101, 366
 Eggen, O. J. 1994, *Galactic and Solar System Optical Astrometry*, 191
 ESA, 1997, *The HIPPARCOS and Tycho Catalogues*, ESA SP-1200
 Famaey, B., Jorissen, A., Luri, X. et al. 2005, *A&A*, 430, 165
 Famaey, B., Pont, F., Luri, X. et al. 2007, *A&A*, 461, 957
 Famaey, B., Siebert, A., & Jorissen, A. 2008, *A&A*, 483, 453
 Francis, C., & Anderson, E. 2009, *Proc. Roy. Soc. Lond. A* 465, 3425
 Francis, C., & Anderson, E. 2009, *New A*, 14, 615
 Freeman, K., & Bland-Hawthorn, J. 2002, *ARA&A*, 40, 487
 Fux, R. 2001, *A&A*, 373, 511
 Ghezzi, L., Cunha, K., Schuler, S. C., & Smith, V. V. 2010, *ApJ*, 725, 721
 Gilli, G., Israelian, G., Ecuivillon, A., Santos, N. C., & Mayor, M. 2006, *A&A*, 449, 723
 González Hernández, J. I., & Bonifacio, P. 2009, *A&A*, 497, 497
 González Hernández, J. I., Israelian, G., Santos, N. C. et al. 2010, *ApJ*, 720, 1592
 González Hernández, J. I., Delgado-Mena, E., Sousa, S. G., et al. 2013, *A&A*, 552, A6
 Høg, E., Fabricius, C., Makarov, V. V., et al. 2000, *A&A*, 355, L27
 Holmberg, J., Nordström, B., & Andersen, J. 2009, *A&A*, 501, 941
 Horne, K. 1986, *PASP*, 98, 609
 Johnson, D. R. H., & Soderblom, D. R. 1987, *AJ*, 93, 864

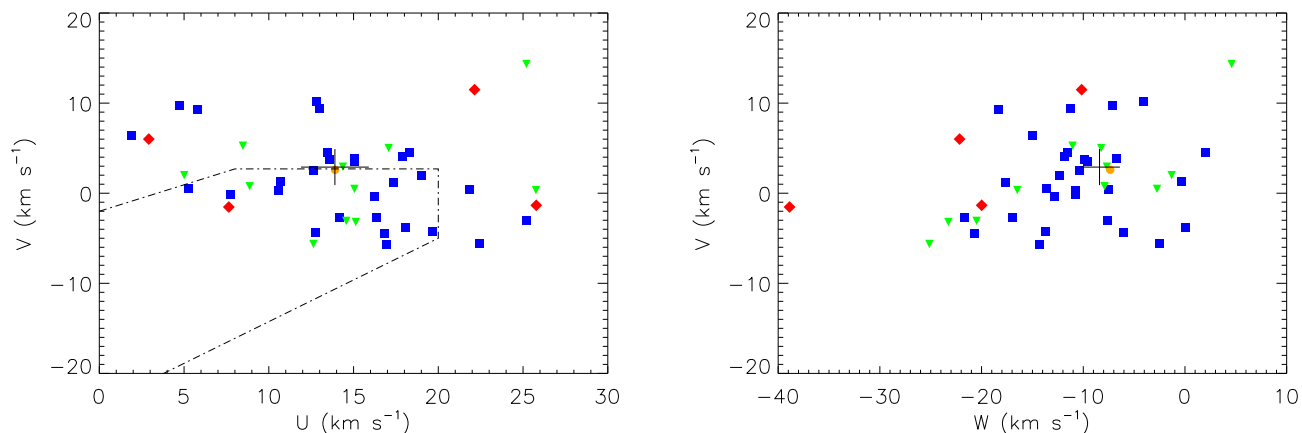


Fig. 7. U , V , and W recalculated velocities for the possible members of the Ursa Major MG. For a full explanation on the final selection criterion, we refer the reader to Section 5. The big black cross indicates the U , V , and W central location of the Ursa Major MG (see King et al. 2003). Dashed lines show the region where the majority of the young disc stars tends to be according to Eggen (1984, 1989). The meaning of the symbols is the same as in Fig. 5

King, J. R., Villarreal, A. R., Soderblom, D. R., Gulliver, A. F., & Adelman, S. J. 2003, *AJ*, 125, 1980
 King, J. R., & Schuler, S. C. 2005, *PASP*, 117, 911
 Klement, R., Fuchs, B., & Rix, H.-W. 2008, *ApJ*, 685, 261
 Koen, C., Kilkenny, D., van Wyk, F., & Marang, F. 2010, *MNRAS*, 403, 1949
 Kurucz, R. L., Furenlid, I., Brault, J., & Testerman, L. 1984, *National Solar Observatory Atlas, Sunspot*, New Mexico: National Solar Observatory, 1984.
 Kurucz, R. L. 1993, *ATLAS9 Stellar Atmosphere Programs and 2 km s⁻¹ grid*. Kurucz CD-ROM No. 13. Cambridge, Mass.: Smithsonian Astrophysical Observatory, 1993., 13,
 Lai, D. K., Bolte, M., Johnson, J. A., et al. 2008, *ApJ*, 681, 1524
 López-Santiago, J., Montes, D., Crespo-Chacón, I., & Fernández-Figueroa, M. J. 2006, *ApJ*, 643, 1160
 López-Santiago, J., Micela, G., & Montes, D. 2009, *A&A*, 499, 129
 López-Santiago, J., Montes, D., Gálvez-Ortiz, M. C. et al. 2010, *A&A*, 514, A97
 Maldonado, J., Martínez-Arnáiz, R. M., Eiroa, C., Montes, D., & Montesinos, B. 2010, *A&A*, 521, A12
 Mamajek, E. E., Meyer, M. R., & Liebert, J. 2002, *AJ*, 124, 1670
 Martínez-Arnáiz, R., Maldonado, J., Montes, D., Eiroa, C., & Montesinos, B. 2010, *A&A*, 520, A79
 McCall, M. L. 2004, *AJ*, 128, 2144
 McLean, I. S. 1997, *Electronic imaging in astronomy. Detectors and instrumentation*, Publisher: Chichester, UK Wiley, 1997 Physical description xxx, 472 p. Series Wiley-PRAXIS series in astronomy and astrophysics Published in association with Praxis Publishing, Chichester ISBN0471969710,
 Mermilliod, J.-C., Mermilliod, M., & Hauck, B. 1997, *A&AS*, 124, 349
 Minchev, I., Boily, C., Siebert, A., & Bienayme, O. 2010, *MNRAS*, 407, 2122
 Minchev, I., & Famaey, B. 2010, *ApJ*, 722, 112
 Mitschang, A. W., De Silva, G., Sharma, S., & Zucker, D. B. 2013, *MNRAS*, 428, 2321
 Montes, D., López-Santiago, J., Gálvez, M. C. et al. 2001a, *MNRAS*, 328, 45
 Montes, D., López-Santiago, J., Fernández-Figueroa, M. J., & Gálvez, M. C. 2001b, *A&A*, 379, 976
 Monier, R. 2005, *A&A*, 442, 563
 Mortier, A., Santos, N. C., Sousa, S. G., et al. 2013, *A&A*, 557A, 70M
 Neves, V., Santos, N. C., Sousa, S. G., Correia, A. C. M., & Israelian, G. 2009, *A&A*, 497, 563
 Paulson, D. B., Sneden, C., & Cochran, W. D. 2003, *AJ*, 125, 3185
 Perryman, M. A. C., Lindgren, L., Kovalevsky, J., et al. 1997, *A&A*, 323, L49
 Pompéia, L., Masseron, T., Famaey, B., et al. 2011, *MNRAS*, 415, 1138
 Press, W. H., Teukolsky, S. A., Vetterling, W. T., & Flannery, B. P. 1992, *Cambridge: University Press*, |c1992, 2nd ed.,
 Quillen, A. C. 2003, *AJ*, 125, 785
 Quillen, A. C., & Minchev, I. 2005, *AJ*, 130, 576
 Raskin, G., van Winckel, H., Hensberge, H., et al. 2011, *A&A*, 526, A69
 Reddy, B. E., Lambert, D. L., & Allende Prieto, C. 2006, *MNRAS*, 367, 1329
 Schlegel, D. J., Finkbeiner, D. P., & Davis, M. 1998, *ApJ*, 500, 525
 Skrutskie, M. F., Cutri, R. M., Stiening, R., et al. 2006, *AJ*, 131, 1163
 Sneden, C. A. 1973, Ph.D. Thesis,
 Soderblom, D. R., & Mayor, M. 1993, *AJ*, 105, 226
 Sousa, S. G., Santos, N. C., Israelian, G., Mayor, M., & Monteiro, M. J. P. F. G. 2007, *A&A*, 469, 783
 Sousa, S. G., Santos, N. C., Mayor, M., et al. 2008, *A&A*, 487, 373

Tabernero, H. M., Montes, D., & González Hernández, J. I. 2012, *A&A*, 547, A13
 Tsantaki, M., Sousa, S. G., Adibekyan, V. Z., et al. 2013, *A&A*, 555, A150
 Tonry, J., & Davis, M. 1979, *AJ*, 84, 1511
 Torres, G., Fischer, D. A., Sozzetti, A., et al. 2012, *ApJ*, 757, 161
 van Leeuwen, F. 2007, *A&A*, 474, 653
 Wielen, R. 1971, *Ap&SS*, 13, 300
 Williams, M. E. K., Freeman, K. C., Helmi, A., & the RAVE collaboration 2009, *IAU Symposium*, 254, 139
 Zhao, J., Zhao, G., & Chen, Y. 2009, *ApJ*, 692, L113

Appendix A: On-line material

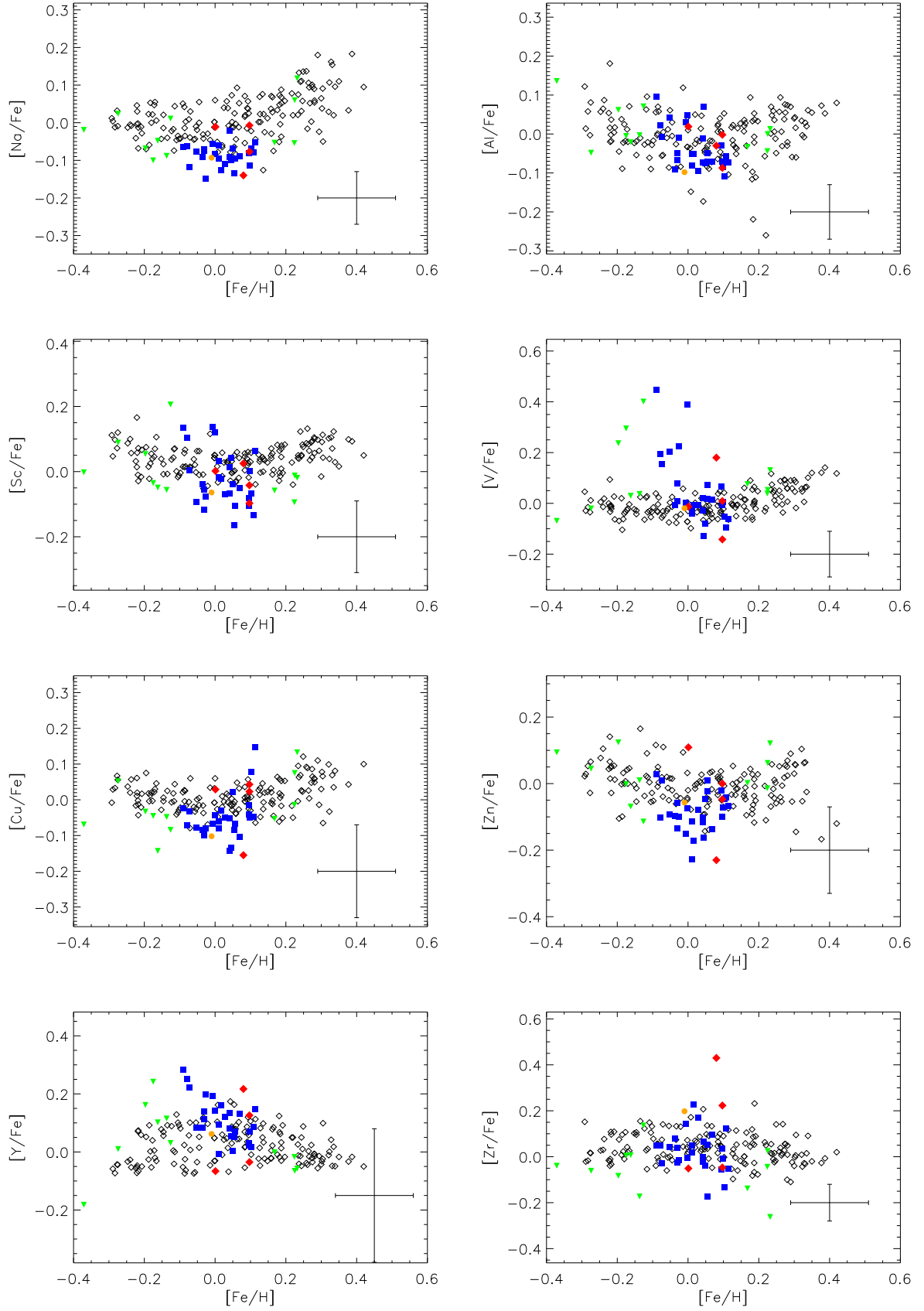


Fig. A.1. Same as Fig. 5 but for the odd-Z elements (Na, Al, Sc, and V), Cu, Zn, and the s-process elements (Y, Zr, Ba, Ce, and Nd).

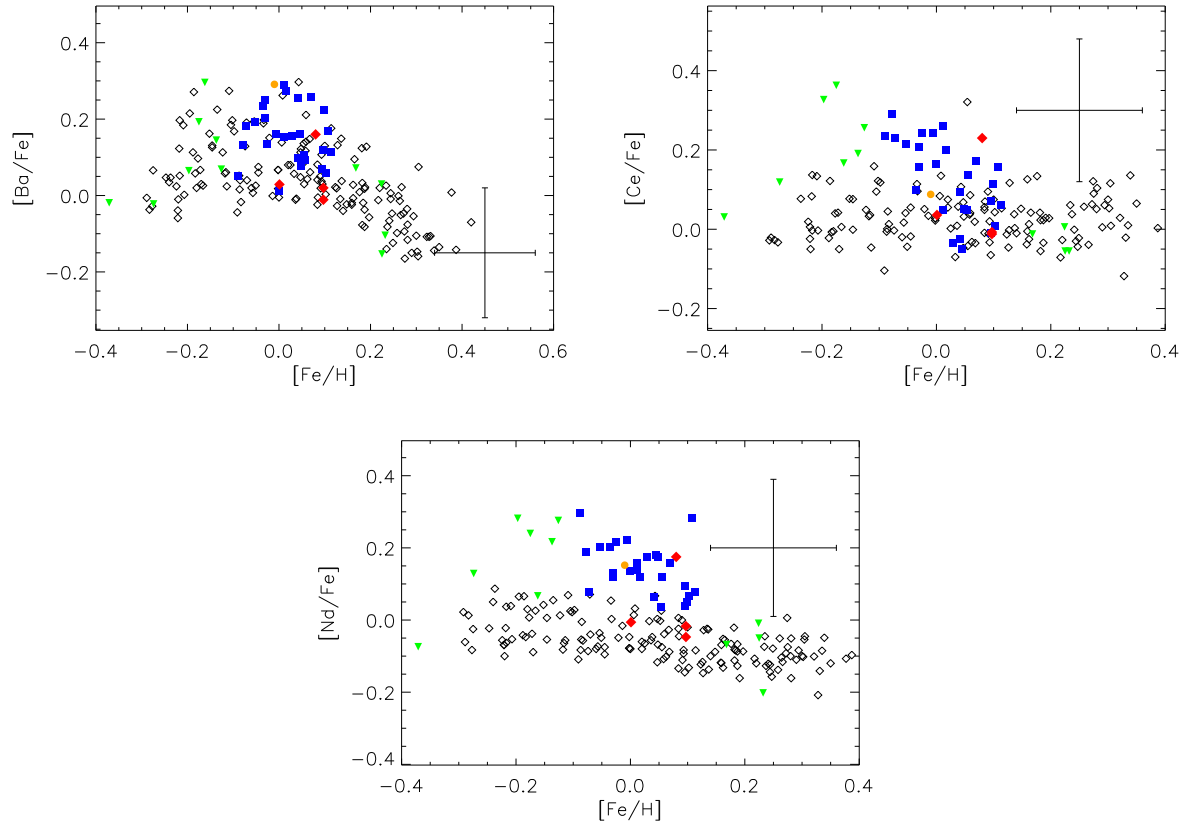


Fig. A.2. Fig. A.1 Continued.

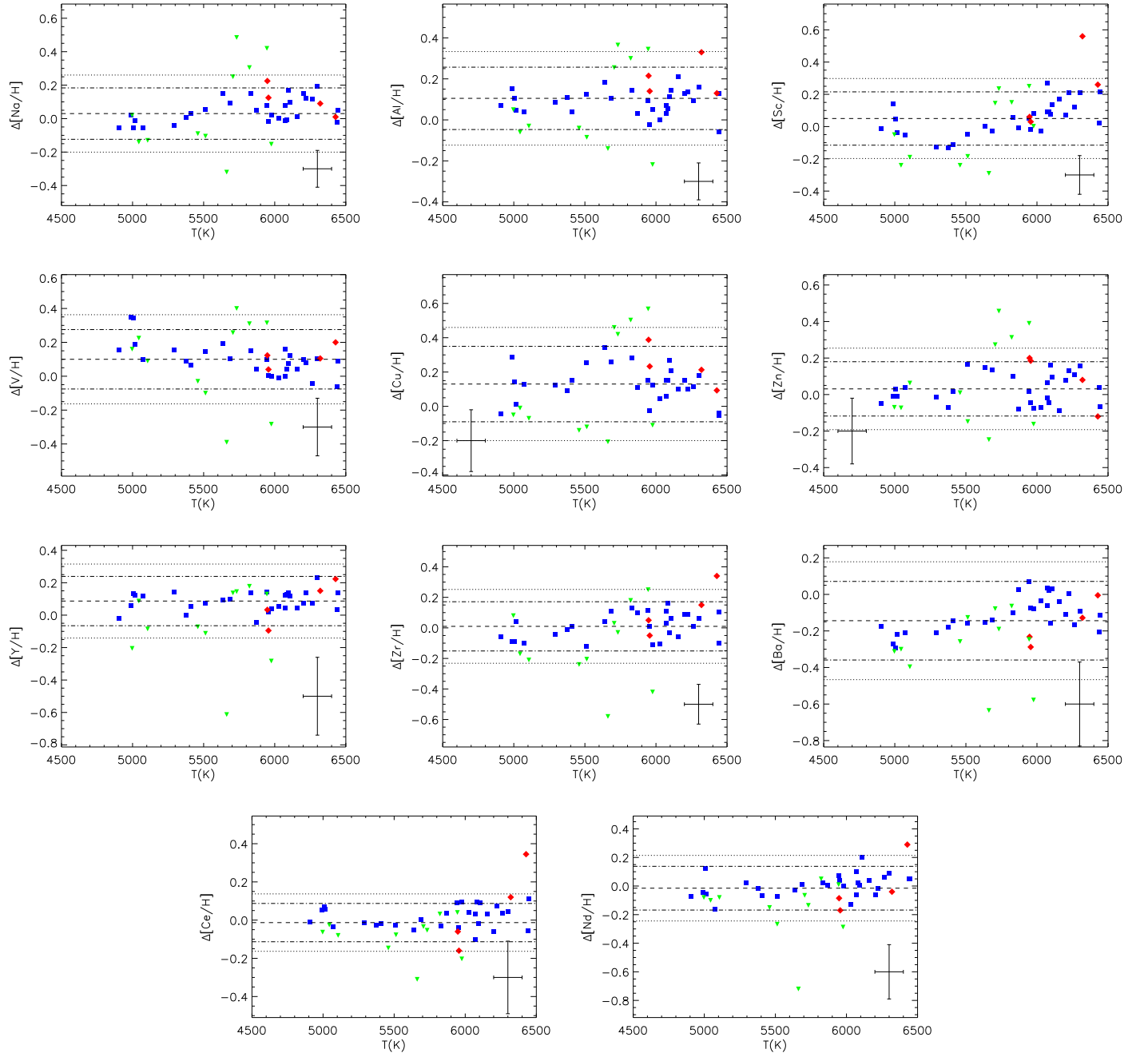


Fig. A.3. Same as Fig. 6 but for the odd-Z elements (Na, Al, Sc, and V), Cu, Zn, and the s-process elements (Y, Zr, Ba, Ce, and Nd).

Table A.2. Wavelength, elements, excitation potential, oscillator strengths for the spectral lines used in the present work. For the Fe_{I,II} linelist, please see Sousa et al. (2008) **References.** (G10) González Hernández et al. (2010); (P11) Pompéia et al. (2011)

λ (Å)	Chemical species	χ_1 (eV)	$\log gf$	Ref.
6154.23	Na I	2.10	-1.622	G10
6160.75	Na I	2.10	-1.363	G10
4730.04	Mg I	4.35	-2.234	G10
5711.09	Mg I	4.35	-1.777	G10
6319.24	Mg I	5.11	-2.300	G10
6696.03	Al I	3.14	-1.571	G10
6698.67	Al I	3.14	-1.886	G10
5517.54	Si I	5.08	-2.496	G10
5645.61	Si I	4.93	-2.068	G10
5684.49	Si I	4.95	-1.642	G10
5701.11	Si I	4.93	-2.034	G10
5753.64	Si I	5.62	-1.333	G10
5772.15	Si I	5.08	-1.669	G10
5797.87	Si I	4.95	-1.912	G10
5948.54	Si I	5.08	-1.208	G10
6125.02	Si I	5.61	-1.555	G10
6142.49	Si I	5.62	-1.520	G10
6145.02	Si I	5.62	-1.425	G10
6195.46	Si I	5.87	-1.666	G10
6237.33	Si I	5.61	-1.116	G10
6243.82	Si I	5.62	-1.331	G10
6244.48	Si I	5.62	-1.310	G10
6527.21	Si I	5.87	-1.227	G10
6721.85	Si I	5.86	-1.156	G10
6741.63	Si I	5.98	-1.625	G10
5261.71	Ca I	2.52	-0.677	G10
5349.47	Ca I	2.71	-0.581	G10
5512.98	Ca I	2.93	-0.559	G10
5867.56	Ca I	2.93	-1.592	G10
6156.02	Ca I	2.52	-2.497	G10
6161.29	Ca I	2.52	-1.313	G10
6166.44	Ca I	2.52	-1.155	G10
6169.04	Ca I	2.52	-0.800	G10
6449.82	Ca I	2.52	-0.733	G10
6455.60	Ca I	2.52	-1.404	G10
6471.67	Ca I	2.53	-0.825	G10
6499.65	Ca I	2.52	-0.917	G10
4743.82	Sc I	1.45	0.297	G10
5520.50	Sc I	1.87	0.562	G10
5671.82	Sc I	1.45	0.533	G10
5526.82	Sc II	1.77	0.140	G10
5657.88	Sc II	1.51	-0.326	G10
5667.14	Sc II	1.50	-1.025	G10
5684.19	Sc II	1.51	-0.946	G10
6245.62	Sc II	1.51	-1.022	G10
6320.84	Sc II	1.50	-1.863	G10
4555.49	Ti I	0.85	-0.575	G10
4562.63	Ti I	0.02	-2.718	G10
4645.19	Ti I	1.73	-0.666	G10
4656.47	Ti I	0.00	-1.308	G10
4675.11	Ti I	1.07	-0.939	G10
4722.61	Ti I	1.05	-1.433	G10
4820.41	Ti I	1.50	-0.429	G10
4913.62	Ti I	1.87	0.068	G10
4997.10	Ti I	0.00	-2.174	G10
5016.17	Ti I	0.85	-0.657	G10
5039.96	Ti I	0.02	-1.199	G10

λ (Å)	Chemical species	χ_1 (eV)	$\log gf$	Ref.
5064.06	Ti I	2.69	-0.471	G10
5071.49	Ti I	1.46	-0.797	G10
5113.44	Ti I	1.44	-0.861	G10
5145.47	Ti I	1.46	-0.622	G10
5219.70	Ti I	0.02	-2.254	G10
5490.16	Ti I	1.46	-1.008	G10
5503.90	Ti I	2.58	-0.218	G10
5648.57	Ti I	2.49	-0.410	G10
5662.16	Ti I	2.32	-0.123	G10
5739.48	Ti I	2.25	-0.781	G10
5766.33	Ti I	3.29	0.326	G10
5965.84	Ti I	1.88	-0.492	G10
5978.55	Ti I	1.87	-0.602	G10
6064.63	Ti I	1.05	-1.941	G10
6091.18	Ti I	2.27	-0.445	G10
6126.22	Ti I	1.07	-1.416	G10
6258.11	Ti I	1.44	-0.435	G10
6261.10	Ti I	1.43	-0.491	G10
6599.12	Ti I	0.90	-2.069	G10
4583.41	Ti II	1.16	-2.840	G10
4636.33	Ti II	1.16	-3.152	G10
4657.20	Ti II	1.24	-2.379	G10
4708.67	Ti II	1.24	-2.392	G10
4911.20	Ti II	3.12	-0.537	G10
5211.54	Ti II	2.59	-1.490	G10
5381.03	Ti II	1.57	-1.904	G10
5418.77	Ti II	1.58	-2.104	G10
5670.85	V I	1.08	-0.482	G10
5727.05	V I	1.08	-0.015	G10
6039.73	V I	1.06	-0.747	G10
6081.45	V I	1.05	-0.692	G10
6090.21	V I	1.08	-0.150	G10
6119.53	V I	1.06	-0.451	G10
6243.11	V I	0.30	-1.067	G10
6251.83	V I	0.29	-1.431	G10
4575.11	Cr I	3.37	-1.004	G10
4626.18	Cr I	0.97	-1.467	G10
4633.25	Cr I	3.13	-1.215	G10
4700.61	Cr I	2.71	-1.464	G10
4708.02	Cr I	3.17	-0.104	G10
4730.72	Cr I	3.08	-0.345	G10
4767.86	Cr I	3.56	-0.599	G10
4801.03	Cr I	3.12	-0.251	G10
4936.34	Cr I	3.11	-0.343	G10
5122.12	Cr I	1.03	-3.166	G10
5214.14	Cr I	3.37	-0.784	G10
5238.97	Cr I	2.71	-1.427	G10
5247.57	Cr I	0.96	-1.618	G10
5287.18	Cr I	3.44	-0.954	G10
5348.33	Cr I	1.00	-1.229	G10
5480.51	Cr I	3.45	-0.997	G10
5781.18	Cr I	3.32	-0.886	G10
5783.07	Cr I	3.32	-0.472	G10
5787.92	Cr I	3.32	-0.183	G10
6882.52	Cr I	3.44	-0.392	G10
4588.20	Cr II	4.07	-0.752	G10
4592.05	Cr II	4.07	-1.252	G10
4884.61	Cr II	3.86	-2.069	G10
4502.21	Mn I	2.92	-0.523	G10
4739.11	Mn I	2.94	-0.462	G10
4761.51	Mn I	2.95	-0.147	G10
5377.62	Mn I	3.84	-0.068	G10

λ (Å)	Chemical species	χ_1 (eV)	$\log gf$	Ref.
6013.49	Mn I	3.07	0.046	G10
4594.63	Co I	3.63	-0.279	G10
4792.86	Co I	3.25	-0.080	G10
4813.48	Co I	3.22	0.177	G10
5301.05	Co I	1.71	-1.950	G10
5342.71	Co I	4.02	0.606	G10
5352.05	Co I	3.58	0.004	G10
5359.20	Co I	4.15	0.040	G10
5647.24	Co I	2.28	-1.594	G10
6814.95	Co I	1.96	-1.822	G10
4512.99	Ni I	3.71	-1.467	G10
4811.99	Ni I	3.66	-1.363	G10
4814.60	Ni I	3.60	-1.670	G10
4913.98	Ni I	3.74	-0.661	G10
4946.04	Ni I	3.80	-1.224	G10
4952.29	Ni I	3.61	-1.261	G10
4976.33	Ni I	1.68	-3.002	G10
4995.66	Ni I	3.63	-1.611	G10
5010.94	Ni I	3.63	-0.901	G10
5081.11	Ni I	3.85	0.064	G10
5094.41	Ni I	3.83	-1.108	G10
5392.33	Ni I	4.15	-1.354	G10
5435.86	Ni I	1.99	-2.432	G10
5462.50	Ni I	3.85	-0.880	G10
5587.87	Ni I	1.93	-2.479	G10
5589.36	Ni I	3.90	-1.148	G10
5625.32	Ni I	4.09	-0.731	G10
5628.35	Ni I	4.09	-1.316	G10
5638.75	Ni I	3.90	-1.699	G10
5641.88	Ni I	4.11	-1.017	G10
5643.08	Ni I	4.16	-1.234	G10
5694.99	Ni I	4.09	-0.629	G10
5748.36	Ni I	1.68	-3.279	G10
5805.22	Ni I	4.17	-0.604	G10
5847.00	Ni I	1.68	-3.410	G10
5996.73	Ni I	4.24	-1.010	G10
6086.29	Ni I	4.27	-0.471	G10
6108.12	Ni I	1.68	-2.512	G10
6111.08	Ni I	4.09	-0.823	G10
6119.76	Ni I	4.27	-1.316	G10
6128.98	Ni I	1.68	-3.368	G10
6130.14	Ni I	4.27	-0.938	G10
6175.37	Ni I	4.09	-0.534	G10
6176.82	Ni I	4.09	-0.266	G10
6177.25	Ni I	1.83	-3.538	G10
6186.72	Ni I	4.11	-0.888	G10
6204.61	Ni I	4.09	-1.112	G10
6223.99	Ni I	4.11	-0.954	G10
6230.10	Ni I	4.11	-1.132	G10
6322.17	Ni I	4.15	-1.164	G10
6327.60	Ni I	1.68	-3.086	G10
6360.81	Ni I	4.17	-1.145	G10
6378.26	Ni I	4.15	-0.830	G10
6598.60	Ni I	4.24	-0.914	G10
6635.13	Ni I	4.42	-0.779	G10
6767.78	Ni I	1.83	-2.136	G10
6772.32	Ni I	3.66	-0.963	G10
6842.04	Ni I	3.66	-1.496	G10
5105.55	Cu I	1.39	-1.520	G10
5218.21	Cu I	3.82	0.480	G10
5220.09	Cu I	3.82	-0.450	G10
5782.12	Cu I	1.64	-1.720	G10

λ (Å)	Chemical species	χ_1 (eV)	$\log gf$	Ref.
4722.16	Zn I	4.03	-0.370	G10
4810.54	Zn I	4.08	-0.170	G10
6362.35	Zn I	5.79	0.140	G10
4900.12	Y II	1.03	-0.090	G10
5087.43	Y II	1.08	-0.160	G10
5200.42	Y II	0.99	-0.570	G10
5402.78	Y II	1.84	-0.440	G10
4687.81	Zr I	0.73	0.550	P11
4739.48	Zr I	0.65	0.230	P11
5112.28	Zr II	1.66	-0.590	G10
4554.03	Ba II	0.00	0.140	P11
4934.08	Ba II	0.00	-0.157	P11
5853.67	Ba II	0.60	-0.909	G10
6141.71	Ba II	0.70	-0.030	G10
6496.90	Ba II	0.60	-0.406	G10
4523.08	Ce II	0.51	0.040	G10
4562.36	Ce II	0.48	0.230	P11
4628.16	Ce II	0.52	0.230	G10
4773.96	Ce II	0.92	0.250	G10
5274.23	Ce II	1.04	0.150	G10
5092.80	Nd II	0.38	-0.650	G10
5319.82	Nd II	0.55	-0.140	P11

Table A.4. [X/Fe] ratios for the s-process elements: Cu, Zn, Y, Zr, Ba, Ce, and Nd. Their uncertainties are the line-to-line dispersion.

Name	Instrument ^a	[Cu/Fe]	[Zn/Fe]	[Y/Fe]	[Zr/Fe]	[Ba/Fe]	[Ce/Fe]	[Nd/Fe]
HD 115043	H, T	-0.10 ± 0.11	-0.06 ± 0.05	0.06 ± 0.05	0.08 ± 0.10	0.29 ± 0.05	0.09 ± 0.04	0.15 ± 0.03
HD 4048	T	-0.16 ± 0.12	-0.23 ± 0.08	0.22 ± 0.01	0.20 ± —	0.16 ± 0.17	0.23 ± 0.14	0.17 ± 0.01
V445 And	F, T	-0.10 ± 0.04	-0.14 ± 0.04	0.14 ± 0.05	-0.14 ± —	0.25 ± 0.05	0.16 ± 0.06	0.12 ± 0.01
HD 8004	T	-0.05 ± 0.03	-0.08 ± 0.04	0.12 ± 0.01	-0.06 ± —	0.16 ± 0.01	-0.03 ± 0.13	0.18 ± 0.01
HD 13829	T	-0.14 ± 0.01	-0.16 ± 0.07	0.05 ± 0.07	-0.16 ± —	0.16 ± 0.04	-0.05 ± 0.10	0.18 ± 0.01
HD 20367	T	-0.05 ± 0.08	-0.04 ± 0.12	0.09 ± 0.05	-0.11 ± —	0.17 ± 0.04	-0.05 ± 0.07	0.21 ± 0.05
γ Lep A	H	-0.07 ± 0.01	-0.03 ± 0.02	0.10 ± 0.04	-0.06 ± —	0.15 ± 0.06	0.18 ± 0.09	0.25 ± 0.16
γ Lep B	H	0.01 ± 0.03	-0.05 ± 0.03	0.03 ± 0.08	0.05 ± —	0.25 ± 0.10	0.30 ± 0.04	0.20 ± 0.01
V1386 Ori	H	-0.08 ± 0.04	-0.10 ± 0.03	0.20 ± 0.12	-0.01 ± —	0.13 ± 0.08	0.24 ± 0.02	0.22 ± 0.22
HD 51419	T	-0.07 ± 0.05	0.09 ± 0.04	-0.18 ± 0.01	-0.27 ± —	-0.02 ± 0.04	0.03 ± 0.01	-0.07 ± 0.01
HD 56168	H	-0.05 ± 0.04	-0.00 ± 0.08	0.24 ± 0.24	0.00 ± —	0.19 ± 0.07	0.36 ± 0.02	0.24 ± 0.10
DX Lyn	H	-0.03 ± 0.01	0.01 ± 0.03	0.22 ± 0.13	-0.03 ± —	0.18 ± 0.08	0.23 ± 0.07	0.08 ± 0.09
V869 Mon	F, T	-0.02 ± 0.09	0.03 ± 0.08	0.28 ± 0.15	-0.07 ± —	0.05 ± 0.05	0.24 ± 0.03	0.30 ± 0.02
HD 64942	F	-0.06 ± —	-0.23 ± 0.18	-0.01 ± 0.12	0.02 ± —	0.29 ± 0.07	0.26 ± 0.05	0.16 ± 0.06
HD 72659	H	0.03 ± 0.06	0.11 ± 0.04	-0.07 ± 0.02	-0.05 ± —	0.03 ± 0.03	0.04 ± 0.02	-0.01 ± 0.14
II Cnc	H	-0.09 ± 0.00	-0.06 ± 0.01	0.11 ± 0.03	0.04 ± —	0.20 ± 0.06	0.21 ± 0.05	0.13 ± 0.15
HD 76218	H	-0.08 ± 0.05	-0.09 ± 0.01	0.08 ± 0.05	0.04 ± —	0.19 ± 0.08	0.22 ± 0.03	0.20 ± 0.08
HD 81659	H	-0.05 ± 0.06	0.00 ± 0.01	-0.00 ± 0.04	-0.14 ± —	0.07 ± 0.03	-0.01 ± 0.05	-0.07 ± 0.12
HD 91148	H	-0.04 ± 0.04	-0.02 ± 0.00	0.03 ± 0.03	-0.05 ± —	0.07 ± 0.04	-0.01 ± 0.06	0.04 ± 0.08
HD 91204	H	0.08 ± 0.01	0.06 ± 0.03	-0.06 ± 0.04	0.03 ± —	-0.15 ± 0.10	-0.05 ± 0.03	-0.05 ± 0.20
HD 93215	H	-0.01 ± 0.08	-0.01 ± 0.06	-0.02 ± 0.01	-0.04 ± —	0.03 ± 0.03	0.01 ± 0.05	-0.01 ± 0.12
HD100310	F	-0.05 ± 0.17	0.01 ± 0.02	0.11 ± 0.04	-0.17 ± —	0.14 ± 0.12	0.19 ± 0.04	0.22 ± 0.01
HD104289	H	0.15 ± 0.01	-0.07 ± 0.10	0.15 ± 0.08	-0.05 ± —	0.12 ± 0.04	0.06 ± 0.03	0.08 ± 0.01
DO CVn	F	-0.07 ± —	-0.10 ± —	0.25 ± 0.19	0.05 ± —	0.13 ± 0.09	0.29 ± 0.03	0.19 ± 0.08
NP UMa	F	-0.08 ± —	-0.11 ± —	0.03 ± 0.05	0.14 ± —	0.07 ± 0.09	0.26 ± 0.03	0.28 ± 0.01
HD 116497	H	-0.05 ± 0.03	-0.07 ± 0.04	0.07 ± 0.04	-0.01 ± —	0.22 ± 0.02	0.11 ± 0.03	0.05 ± 0.03
HN Boo	H, T	-0.04 ± 0.09	-0.07 ± 0.05	0.14 ± 0.20	-0.12 ± —	0.01 ± 0.05	0.17 ± 0.06	0.14 ± 0.12
HP Boo	F	-0.14 ± —	-0.11 ± 0.01	0.13 ± 0.01	-0.00 ± —	0.26 ± 0.05	0.09 ± 0.05	0.06 ± 0.04
ξ Boo	F, T	-0.14 ± 0.02	-0.07 ± 0.04	0.10 ± 0.04	-0.11 ± —	0.30 ± 0.09	0.17 ± 0.04	0.07 ± 0.17
HD 135143	H	0.08 ± 0.07	-0.05 ± 0.01	0.02 ± 0.03	-0.13 ± —	0.06 ± 0.05	0.01 ± 0.05	0.07 ± 0.11
AN CrB	F	-0.03 ± —	0.12 ± 0.17	0.16 ± 0.13	-0.08 ± —	0.06 ± 0.14	0.33 ± 0.06	0.28 ± 0.01
HD 150706	H, F, T	-0.08 ± 0.05	-0.10 ± 0.06	0.08 ± 0.02	0.00 ± —	0.23 ± 0.03	0.10 ± 0.05	0.20 ± 0.07
HD 151044	F	-0.05 ± 0.00	-0.10 ± 0.03	0.08 ± 0.01	-0.02 ± —	0.10 ± 0.02	-0.01 ± 0.04	0.06 ± 0.03
HD 153458	H	-0.02 ± 0.02	-0.10 ± 0.02	0.02 ± 0.01	0.03 ± —	0.12 ± 0.03	0.07 ± 0.01	0.09 ± 0.14
HD 153637	H, T	0.05 ± 0.08	0.04 ± 0.20	0.01 ± 0.07	-0.18 ± —	-0.02 ± 0.07	0.12 ± 0.12	0.13 ± 0.09
HD 162209	H	0.04 ± 0.06	0.00 ± 0.03	-0.04 ± 0.03	-0.05 ± —	-0.01 ± 0.04	-0.01 ± 0.01	-0.02 ± 0.01
HD 163183	H, T	-0.03 ± 0.01	-0.17 ± 0.05	0.16 ± 0.11	0.11 ± —	0.27 ± 0.03	0.13 ± 0.04	0.12 ± 0.01
HD 167043	H	0.02 ± 0.04	-0.05 ± 0.05	0.00 ± 0.02	-0.04 ± —	0.08 ± 0.04	0.05 ± 0.04	0.18 ± 0.05
HD 167389	T	-0.08 ± 0.01	-0.11 ± 0.07	0.09 ± 0.03	-0.18 ± —	0.15 ± 0.03	0.05 ± 0.09	0.14 ± 0.01
HD 181655	H	-0.07 ± 0.03	-0.02 ± 0.01	0.07 ± 0.02	0.05 ± —	0.09 ± 0.07	0.14 ± 0.02	0.12 ± 0.04
HD 184385	H	-0.08 ± 0.06	0.01 ± 0.05	0.05 ± 0.03	-0.17 ± —	0.11 ± 0.03	0.05 ± 0.04	0.04 ± 0.10
HD 184960	H, F, T	-0.07 ± 0.03	-0.15 ± 0.06	0.19 ± 0.07	0.07 ± —	0.16 ± 0.05	0.24 ± 0.09	0.22 ± 0.03
HD 188015	H	0.13 ± 0.03	0.12 ± 0.04	-0.06 ± 0.01	-0.26 ± —	-0.10 ± 0.04	-0.05 ± 0.11	-0.20 ± 0.09
HD 216625	T	0.02 ± 0.06	-0.05 ± 0.05	0.13 ± 0.04	-0.01 ± —	0.02 ± 0.13	-0.01 ± 0.01	-0.05 ± 0.01
MT Peg	F, T	-0.10 ± 0.01	-0.14 ± 0.03	0.13 ± 0.02	-0.02 ± —	0.26 ± 0.04	0.10 ± 0.05	0.16 ± 0.05

Notes. ^(a) Instruments employed to acquire the data: HERMES (H), FOCES (F), and TLS (T).

Table A.6. Differential abundances ($\Delta[X/H]$) with respect to HD 115043 for the s-process elements: Cu, Zn, Y, Zr, Ba, Ce, and Nd. Their uncertainties are the line-to-line dispersion.

Name	Instrument ^a	$\Delta[\text{Cu}/\text{H}]$	$\Delta[\text{Zn}/\text{H}]$	$\Delta[\text{Y}/\text{H}]$	$\Delta[\text{Zr}/\text{H}]$	$\Delta[\text{Ba}/\text{H}]$	$\Delta[\text{Ce}/\text{H}]$	$\Delta[\text{Nd}/\text{H}]$
HD 4048	T	0.09 ± 0.12	-0.12 ± 0.08	0.22 ± 0.01	0.34 ± —	-0.00 ± 0.17	0.34 ± 0.14	0.29 ± 0.01
V445 And	F, T	0.04 ± 0.04	-0.07 ± 0.03	0.05 ± 0.10	-0.10 ± —	-0.03 ± 0.03	0.04 ± 0.03	-0.13 ± 0.01
HD 8004	T	0.15 ± 0.03	-0.02 ± 0.04	0.04 ± 0.01	0.03 ± —	-0.06 ± 0.01	0.03 ± 0.13	0.10 ± 0.01
HD 13829	T	0.10 ± 0.01	-0.09 ± 0.07	0.04 ± 0.07	-0.06 ± —	-0.04 ± 0.04	0.03 ± 0.10	0.04 ± 0.01
HD 20367	T	0.21 ± 0.03	0.10 ± 0.03	0.12 ± 0.08	0.06 ± —	0.03 ± 0.10	0.09 ± 0.04	0.20 ± 0.01
γ Lep A	H	-0.05 ± 0.03	0.04 ± 0.11	0.04 ± 0.08	-0.10 ± —	-0.21 ± 0.04	-0.05 ± 0.02	0.05 ± 0.01
γ Lep B	H	-0.05 ± 0.12	-0.05 ± 0.07	-0.02 ± 0.07	-0.06 ± —	-0.17 ± 0.07	-0.01 ± 0.07	-0.08 ± 0.09
V1386 Ori	H	0.12 ± 0.11	-0.01 ± 0.08	0.14 ± 0.17	-0.04 ± —	-0.21 ± 0.08	-0.01 ± 0.10	0.03 ± 0.16
HD 51419	T	-0.21 ± 0.05	-0.25 ± 0.04	-0.61 ± 0.01	-0.58 ± —	-0.63 ± 0.04	-0.31 ± 0.01	-0.72 ± 0.01
HD 56168	H	-0.01 ± 0.10	-0.07 ± 0.10	0.09 ± 0.31	-0.17 ± —	-0.30 ± 0.06	-0.03 ± 0.09	-0.10 ± 0.04
DX Lyn	H	0.13 ± 0.13	0.04 ± 0.06	0.12 ± 0.19	-0.10 ± —	-0.21 ± 0.08	-0.03 ± 0.08	-0.16 ± 0.03
V869 Mon	F, T	0.14 ± 0.09	0.03 ± 0.08	0.13 ± 0.18	-0.09 ± —	-0.29 ± 0.03	0.07 ± 0.05	0.12 ± 0.05
HD 64942	F	0.11 ± —	-0.08 ± 0.17	-0.05 ± 0.16	0.10 ± —	0.03 ± 0.01	0.04 ± 0.01	0.00 ± 0.12
HD 72659	H	0.23 ± 0.09	0.19 ± 0.05	-0.09 ± 0.07	-0.05 ± —	-0.29 ± 0.03	-0.16 ± 0.07	-0.17 ± 0.07
II Cnc	H	0.15 ± 0.13	0.02 ± 0.04	0.05 ± 0.10	0.01 ± —	-0.14 ± 0.03	-0.02 ± 0.04	-0.06 ± 0.09
HD 76218	H	0.09 ± 0.12	-0.07 ± 0.03	-0.00 ± 0.12	-0.01 ± —	-0.18 ± 0.09	-0.03 ± 0.06	-0.01 ± 0.01
HD 81659	H	0.46 ± 0.17	0.27 ± 0.04	0.14 ± 0.09	0.03 ± —	-0.08 ± 0.03	-0.03 ± 0.02	-0.06 ± 0.05
HD 91148	H	0.34 ± 0.15	0.15 ± 0.02	0.09 ± 0.08	0.04 ± —	-0.15 ± 0.04	-0.05 ± 0.03	-0.03 ± 0.01
HD 91204	H	0.57 ± 0.14	0.39 ± 0.05	0.13 ± 0.07	0.25 ± —	-0.25 ± 0.09	0.04 ± 0.05	0.01 ± 0.14
HD 93215	H	0.50 ± 0.14	0.31 ± 0.09	0.18 ± 0.08	0.18 ± —	-0.06 ± 0.03	0.03 ± 0.04	0.05 ± 0.06
HD 100310	F	-0.14 ± 0.05	0.01 ± 0.01	-0.07 ± 0.11	-0.24 ± —	-0.26 ± 0.05	-0.15 ± 0.07	-0.15 ± 0.01
HD 104289	H	0.18 ± 0.01	0.16 ± 0.05	0.23 ± 0.08	0.06 ± —	-0.09 ± 0.04	0.04 ± 0.08	0.09 ± 0.01
DO CVn	F	0.01 ± —	-0.01 ± —	-0.12 ± 0.25	0.04 ± —	-0.22 ± 0.03	0.06 ± 0.08	-0.05 ± 0.01
NP UMa	F	-0.05 ± —	-0.07 ± —	-0.20 ± 0.09	0.08 ± —	-0.31 ± 0.03	-0.06 ± 0.05	-0.08 ± 0.01
HD 116497	H	0.10 ± 0.05	0.13 ± 0.04	0.14 ± 0.08	0.09 ± —	0.01 ± 0.04	0.08 ± 0.06	-0.01 ± 0.04
HN Boo	H, T	0.29 ± 0.14	-0.01 ± 0.05	0.06 ± 0.18	-0.09 ± —	-0.27 ± 0.04	0.05 ± 0.04	-0.05 ± 0.09
HP Boo	F	0.06 ± —	0.06 ± 0.02	0.12 ± 0.07	0.11 ± —	0.04 ± 0.01	-0.10 ± 0.05	-0.06 ± 0.03
ξ Boo	F, T	-0.12 ± 0.02	-0.15 ± 0.03	-0.11 ± 0.07	-0.20 ± —	-0.13 ± 0.06	-0.08 ± 0.05	-0.27 ± 0.14
HD 135143	H	0.27 ± 0.03	0.16 ± 0.02	0.14 ± 0.09	-0.03 ± —	-0.16 ± 0.05	-0.02 ± 0.03	0.00 ± 0.05
AN CrB	F	-0.07 ± —	0.06 ± 0.15	-0.09 ± 0.20	-0.21 ± —	-0.40 ± 0.07	-0.08 ± 0.14	-0.08 ± 0.06
HD 150706	H, F, T	-0.02 ± 0.05	-0.04 ± 0.04	0.02 ± 0.07	0.01 ± —	-0.08 ± 0.02	-0.04 ± 0.08	0.04 ± 0.05
HD 151044	F	0.15 ± 0.00	0.08 ± 0.01	0.07 ± 0.07	0.09 ± —	-0.11 ± 0.04	-0.06 ± 0.01	-0.06 ± 0.04
HD 153458	H	0.28 ± 0.10	0.10 ± 0.01	0.14 ± 0.09	0.13 ± —	-0.10 ± 0.05	-0.03 ± 0.08	0.03 ± 0.08
HD 153637	H, T	-0.11 ± 0.06	-0.16 ± 0.19	-0.28 ± 0.11	-0.42 ± —	-0.58 ± 0.06	-0.20 ± 0.13	-0.29 ± 0.06
HD 162209	H	0.39 ± 0.12	0.20 ± 0.02	0.03 ± 0.06	0.05 ± —	-0.23 ± 0.03	-0.06 ± 0.12	-0.09 ± 0.06
HD 163183	H, T	0.15 ± 0.01	-0.05 ± 0.04	0.13 ± 0.15	0.16 ± —	0.02 ± 0.02	0.10 ± 0.01	0.03 ± 0.01
HD 167043	H	0.12 ± 0.04	0.11 ± 0.04	0.07 ± 0.09	0.01 ± —	-0.17 ± 0.05	0.04 ± 0.08	0.06 ± 0.02
HD 167389	T	0.12 ± 0.01	-0.07 ± 0.07	0.04 ± 0.03	-0.11 ± —	-0.08 ± 0.03	0.09 ± 0.09	0.00 ± 0.01
HD 181655	H	0.26 ± 0.13	0.14 ± 0.04	0.10 ± 0.07	0.11 ± —	-0.14 ± 0.02	0.00 ± 0.06	0.01 ± 0.03
HD 184385	H	0.25 ± 0.14	0.17 ± 0.08	0.08 ± 0.07	-0.12 ± —	-0.16 ± 0.04	-0.03 ± 0.03	-0.08 ± 0.04
HD 184960	H, F, T	-0.04 ± 0.10	-0.07 ± 0.04	0.14 ± 0.10	0.10 ± —	-0.11 ± 0.06	0.11 ± 0.11	0.05 ± 0.02
HD 188015	H	0.42 ± 0.15	0.46 ± 0.07	0.14 ± 0.08	-0.03 ± —	-0.19 ± 0.02	-0.05 ± 0.13	-0.14 ± 0.03
HD 216625	T	0.21 ± 0.06	0.08 ± 0.05	0.15 ± 0.04	0.15 ± —	-0.13 ± 0.13	0.12 ± 0.01	-0.04 ± 0.01
MT Peg	F, T	0.15 ± 0.01	0.02 ± 0.03	0.14 ± 0.04	0.12 ± —	0.07 ± 0.01	0.09 ± 0.05	0.07 ± 0.02

Notes. ^(a) Instruments employed to acquire the data: HERMES (H), FOCES (F), and TLS (T).

Table A.7. Differential abundance average sensitivities for Fe, Na, Mg, Al, Si, Ca, Sc, Ti, V, Cr, Mn, Co, and Ni.

Name	Δ [Fe/H]	Δ [Na/H]	Δ [Mg/H]	Δ [Al/H]	Δ [Si/H]	Δ [Ca/H]	Δ [Sc/H]	Δ [Ti/H]	Δ [V/H]	Δ [Cr/H]	Δ [Mn/H]	Δ [Co/H]	Δ [Ni/H]
$\Delta T_{\text{eff}} = \pm 100$ K													
HD 64942	0.07	0.08	0.07	0.08	0.03	0.10	0.09	0.14	0.15	0.11	0.12	0.10	0.08
HD 184385	0.06	0.09	0.07	0.08	0.00	0.11	0.10	0.16	0.18	0.12	0.12	0.07	0.06
HD 56168	0.05	0.11	0.06	0.09	0.04	0.14	0.11	0.18	0.21	0.13	0.11	0.04	0.02
Average	0.06	0.09	0.07	0.08	0.02	0.12	0.10	0.16	0.18	0.12	0.12	0.07	0.05
$\Delta \log g = \pm 0.30$ dex													
HD 64942	0.03	0.04	0.04	0.02	0.00	0.10	0.01	0.01	0.01	0.03	0.08	0.01	0.01
HD 184385	0.03	0.05	0.06	0.03	0.03	0.12	0.01	0.02	0.01	0.05	0.11	0.03	0.03
HD 56168	0.02	0.07	0.04	0.03	0.07	0.16	0.01	0.06	0.05	0.07	0.11	0.06	0.06
Average	0.03	0.05	0.05	0.03	0.03	0.13	0.01	0.03	0.02	0.05	0.10	0.03	0.03
$\Delta \xi = \pm 0.50$ km s ⁻¹													
HD 64942	0.07	0.02	0.03	0.01	0.02	0.11	0.01	0.07	0.04	0.08	0.17	0.05	0.06
HD 184385	0.07	0.03	0.04	0.03	0.02	0.11	0.02	0.11	0.11	0.10	0.17	0.07	0.09
HD 56168	0.06	0.02	0.03	0.02	0.01	0.07	0.03	0.15	0.20	0.07	0.11	0.05	0.06
average	0.07	0.02	0.03	0.02	0.02	0.10	0.02	0.13	0.12	0.08	0.15	0.06	0.07
$\Delta[\text{Fe}/\text{H}] = \pm 0.30$ dex													
HD 64942	0.02	0.01	0.00	0.01	0.04	0.03	0.01	0.01	0.01	0.01	0.02	0.02	0.03
HD 184385	0.04	0.02	0.04	0.01	0.07	0.05	0.00	0.00	0.01	0.03	0.07	0.05	0.07
HD 56168	0.08	0.03	0.07	0.02	0.10	0.08	0.00	0.03	0.02	0.06	0.12	0.09	0.11
Average	0.05	0.02	0.04	0.01	0.07	0.05	0.00	0.01	0.01	0.03	0.07	0.05	0.07
$\sigma[\text{X}/\text{H}]$													
HD 64942	0.01	0.01	0.10	0.01	0.01	0.01	0.05	0.01	0.05	0.01	0.02	0.04	0.01
HD 184385	0.01	0.01	0.05	0.03	0.01	0.01	0.05	0.01	0.01	0.01	0.02	0.01	0.01
HD 56168	0.01	0.03	0.14	0.02	0.01	0.01	0.10	0.01	0.03	0.01	0.04	0.01	0.01
Average	0.01	0.02	0.10	0.02	0.01	0.01	0.07	0.01	0.03	0.01	0.03	0.02	0.01
Total	0.11	0.11	0.14	0.09	0.08	0.21	0.12	0.21	0.17	0.16	0.23	0.10	0.12
$\Delta[\text{X}/\text{Fe}]$	—	0.07	0.11	0.07	0.07	0.12	0.11	0.12	0.09	0.07	0.13	0.04	0.02

Notes. Sensitivities to changes of 100 K in T_{eff} , 0.30 dex in $\log g$, 0.50 km s⁻¹ in ξ , and 0.30 dex in [Fe/H]. We verified these sensitivities for the stars HD 64942 (5869 K, 4.63 dex, 1.11 km s⁻¹, 0.01 dex), HD 184385 (5511 K, 4.48 dex, 0.94 km s⁻¹, 0.05 dex), and HD 56168 (5044 K, 4.53 dex, 0.81 km s⁻¹, -0.18 dex).

Table A.8. Differential abundance sensitivities for Cu, Zn, Y, Zr, Ba, Ce, and Nd.

Name	$\Delta[\text{Cu}/\text{H}]$	$\Delta[\text{Zn}/\text{H}]$	$\Delta[\text{Y}/\text{H}]$	$\Delta[\text{Zr}/\text{H}]$	$\Delta[\text{Ba}/\text{H}]$	$\Delta[\text{Ce}/\text{H}]$	$\Delta[\text{Nd}/\text{H}]$
$\Delta T_{\text{eff}} = \pm 100 \text{ K}$							
HD 64942	0.06	0.01	0.01	0.11	0.01	0.03	0.02
HD 184385	0.06	0.01	0.01	0.12	0.01	0.02	0.02
HD 56168	0.04	0.03	0.02	0.14	0.02	0.02	0.03
$\Delta \log g = \pm 0.30 \text{ dex}$							
HD 64942	0.01	0.04	0.12	0.01	0.04	0.13	0.13
HD 184385	0.02	0.03	0.11	0.01	0.03	0.13	0.13
HD 56168	0.00	0.05	0.08	0.01	0.04	0.12	0.13
$\Delta \xi = \pm 0.50 \text{ km s}^{-1}$							
HD 64942	0.08	0.10	0.11	0.02	0.16	0.06	0.02
HD 184385	0.14	0.10	0.15	0.03	0.16	0.09	0.04
HD 56168	0.09	0.06	0.18	0.09	0.11	0.09	0.05
$\Delta[\text{Fe}/\text{H}] = \pm 0.30 \text{ dex}$							
HD 64942	0.03	0.07	0.10	0.00	0.15	0.10	0.11
HD 184385	0.07	0.09	0.11	0.01	0.17	0.11	0.11
HD 56168	0.11	0.10	0.12	0.00	0.19	0.11	0.12

Table A.9. Differential abundance average sensitivities for Cu, Zn, Y, Zr, Ba, Ce, and Nd.

Name	$\Delta[\text{Cu}/\text{H}]$	$\Delta[\text{Zn}/\text{H}]$	$\Delta[\text{Y}/\text{H}]$	$\Delta[\text{Zr}/\text{H}]$	$\Delta[\text{Ba}/\text{H}]$	$\Delta[\text{Ce}/\text{H}]$	$\Delta[\text{Nd}/\text{H}]$
$\Delta T_{\text{eff}} = \pm 100 \text{ K}$							
HD 64942	0.06	0.01	0.01	0.11	0.01	0.03	0.02
HD 184385	0.06	0.01	0.01	0.12	0.01	0.02	0.02
HD 56168	0.04	0.03	0.02	0.14	0.02	0.02	0.03
Average	0.05	0.02	0.01	0.12	0.01	0.02	0.02
$\Delta \log g = \pm 0.30 \text{ dex}$							
HD 64942	0.01	0.04	0.12	0.01	0.04	0.13	0.13
HD 184385	0.02	0.03	0.11	0.01	0.03	0.13	0.13
HD 56168	0.00	0.05	0.08	0.01	0.04	0.12	0.13
Average	0.01	0.04	0.10	0.01	0.04	0.13	0.13
$\Delta \xi = \pm 0.50 \text{ km s}^{-1}$							
HD 64942	0.08	0.10	0.11	0.02	0.16	0.06	0.02
HD 184385	0.14	0.10	0.15	0.03	0.16	0.09	0.04
HD 56168	0.09	0.06	0.18	0.09	0.11	0.09	0.05
Average	0.10	0.09	0.05	0.05	0.14	0.08	0.04
$\Delta[\text{Fe}/\text{H}] = \pm 0.30 \text{ dex}$							
HD 64942	0.03	0.07	0.10	0.00	0.15	0.10	0.11
HD 184385	0.07	0.09	0.11	0.01	0.17	0.11	0.11
HD 56168	0.11	0.10	0.12	0.00	0.19	0.11	0.12
Average	0.07	0.09	0.11	0.00	0.17	0.11	0.11
$\sigma [\text{X}/\text{H}]$							
HD 64942	—	0.17	0.16	—	0.01	0.01	0.12
HD 184385	0.14	0.08	0.07	—	0.04	0.03	0.04
HD 56168	0.10	0.10	0.31	—	0.06	0.09	0.04
Average	0.12	0.12	0.18	—	0.04	0.04	0.07
Total	0.18	0.18	0.24	0.13	0.23	0.19	0.19
$\Delta [\text{X}/\text{Fe}]$	0.13	0.13	0.23	0.08	0.17	0.18	0.19

Notes. Sensitivities to changes of 100 K in T_{eff} , 0.30 dex in $\log g$, 0.50 km s⁻¹ in ξ , and 0.30 dex in [Fe/H]. We verified these sensitivities for the stars HD 64942 (5869 K, 4.63 dex, 1.11 km s⁻¹, 0.01 dex), HD 184385 (5511 K, 4.48 dex, 0.94 km s⁻¹, 0.05 dex), and HD 56168 (5044 K, 4.53 dex, 0.81 km s⁻¹, -0.18 dex).